Signature of the staggered flux state around a superconducting vortex in underdoped cuprates

doi: 10.1103/PhysRevB.65.064526

Signature of the staggered flux state around a superconducting vortex in underdoped cuprates

Jun-ichiro Kishine
Department of Theoretical Studies, Institute for Molecular Science, Okazaki 444-8585, Japan
and Department of Functional Molecular Science, Graduate University for Advanced Studies, Okazaki 444-8585, Japan

Patrick A. Lee and Xiao-Gang Wen
Department of Physics, Massachusetts Institute of Technology, Cambridge, Massachusetts 02139
(Received 28 August 2001; published 23 January 2002)

Based on the SU(2) lattice-gauge-theory formulation of the t-J model, we discuss a possible signature of the unit-cell doubling associated with the staggered-flux (SF) state in the lightly doped spin liquid. Although the SF state appears only dynamically in a uniform d-wave superconducting state, a topological defect [SU(2) vortex] freezes the SF state inside the vortex core. Consequently, the unit-cell doubling shows up in the hopping (χ_{ij}) and pairing (Δ_{ij}) order parameters of physical electrons. We find that whereas the center in the vortex core is a SF state, as one moves away from the core center, a correlated staggered modulation of χ_{ij} and Δ_{ij} becomes predominant. We predict that over the region outside the core and inside the internal gauge-field-penetration depth around a vortex center, the local density of states exhibits a staggered peak-dip (SPD) structure inside the V-shaped profile when measured on the bonds. The SPD structure has its direct origin in the unit-cell doubling associated with the SF core and the robust topological texture, which has little to do with the symmetry of the d-wave order parameter. Therefore the structure may survive the tunneling-matrix-element effects and easily be detected by the scanning-tunnel-microscope experiment.

DOI: 10.1103/PhysRevB.65.064526 PACS number(s): 74.25.Jb, 71.10.Fd, 71.27.+a

I. INTRODUCTION

High-T_c superconductors are doped Mott insulators. Soon after the discovery, Anderson proposed that the strong correlation physics of the doped Mott insulator is well captured by the t-J model. Taking account of competition between the hole kinetic energy xt and the spin-exchange energy J, he proposed that the spin-liquid states formed out of the resonating valence-bond (RVB) singlets are a good starting point to study this model.[1] A standard way of enforcing the constraint of no double occupancy in the t-J model is the slave boson formalism where a physical electron operator $c_{i\sigma}$ with spin σ at the site i is splintered into an auxiliary spin-$\frac{1}{2}$ fermion $f_{i\sigma}$ and charge-1 boson b_i: $c_{i\sigma}=f_{i\sigma}b_i^\dagger$. One way to describe the spin-liquid state is to start from mean-field (MF) decoupling,[2–4] $\Delta_{ij}=\langle \epsilon_{\sigma\bar{\sigma}} f_{i\sigma} f_{i\bar{\sigma}}\rangle$ and $\chi_{ij}=\langle f_{i\sigma}^\dagger f_{i\sigma}\rangle$, which characterize the spin-liquid state formed out of the RVB singlets. The phases of χ_{ij} and Δ_{ij} transform as the lattice gauge fields under local U(1) transformation, which naturally leads us to a U(1) gauge theory.[5–7] At zero doping, the t-J model reduces to an antiferromagnetic Heisenberg model that has an exact local SU(2) gauge symmetry.[8] Then, the translationally invariant solution can be described as a π-flux state[2] or a d-wave pairing state[3] with $|\chi_{ij}|=|\Delta_{ij}|$. These apparently different mean-field *Ansätze* describe exactly the same MF state, since they are just SU(2) gauge equivalent.

In the U(1) slave-boson formulation, however, the SU(2) symmetry is broken upon hole doping due to the appearance of the boson-hopping term. Consequently, the d-wave superconducting (SC) state and the flux state are no longer equivalent. For small doping and small J/t, the π-flux phase at zero doping is disfavored against the staggered-flux (SF) phase with $|\chi_{ij}|>|\Delta_{ij}|$.[8–10] The SF state, however, breaks physical symmetries associated with the time reversal and the spatial translation, which causes the *unit-cell doubling* and *staggered orbital currents* of the physical holes. Eventually the SC phase is picked out as the MF solution out of a infinite number of degenerate states upon doping.[3,4,11] However, it is still quite natural to expect that the SF state is nearly degenerate with the SC state in the lightly doped spin-liquid states. That is to say, as far as we confine ourselves to the spin-liquid state, the SU(2) gauge structure at zero doping may still be useful to describe the low-energy states in the underdoped regime, which are missing in the U(1) formulation. To substantiate this idea, Wen and Lee[12,13] introduced an SU(2) boson doublet $(h_i)^T=(b_{i1},b_{i2})$ and constructed an effective model, which recovers local SU(2) symmetry even upon doping. From this viewpoint, the SF state plays a crucial role to describe the low-energy spectrum of the lightly doped spin-liquid state. The question that we must consider next is *how to detect a signature of the SF state contained in the low-energy excitation spectrum*. The first step in this direction was addressed by Ivanov, Lee, and Wen[14] who found a signature of the staggered current-current correlation by using a Gutzwiller-projected d-wave pairing wave function. This is naturally interpreted as a consequence of the quantum fluctuations around the SC state toward the SF state. Leung[15] further sought for a signature of the SF state and found the current-current correlation in the d-wave SC state by using exact diagonalization of the t-J model for a system with two holes on a 32-site lattice.

In the experimental side, structure of the low-energy excitations in the underlying ''normal'' metallic phase is concealed by a phase transition to bulk superconductivity. One promising way to escape from this situation is to introduce the topological defect into the superconducting phase, i.e., the vortex. Inside the vortex core, low-energy properties of

the normal metallic phase show up against the surrounding superconducting phase. Remarkable progress in the low-temperature scanning tunnel microscope (STM) technique with atomic resolution[16] has given us good opportunities to look into the electronic states around the superconducting vortex.[17–19] Recent STM experiments[18,19] on $Bi_2Sr_2CaCu_2O_8$ (BSCCO) revealed the striking fact that the normal core-electronic state exhibits the ''pseudogap'' structure characteristic of the normal-state pseudogap above T_c. A description of a vortex core based on conventional BCS theory requires that the superconducting order parameter vanishes inside the core, which is usually accompanied by the vanishing of the energy gap. The experimental finding thus strongly suggests that the electronic structure of the vortex core is qualitatively different from that given by conventional picture.

The theoretical description of the normal core in the light of the strong correlation physics, however, remains unresolved.[20–26] In the SU(2) picture, since the SF state is nearly degenerate with the SC state, it is naturally expected that by frustrating the SC state, the SF state will be revealed inside the core. Based on this idea, Lee and Wen[27] proposed a model of the vortex with a SF core, characterized by a pseudogap and staggered orbital current. Quite recently, Han and co-workers found evidence of the SF order near the vortex core by using the Gutzwiller projected U(1) slave-boson mean-field wave function.[25,26] These numerical results so far[14,15,25,26] strongly suggest that the SF state is a key ingredient in the t-J model.

The vortex with the SF core [SU(2) vortex] offers us an opportunity to experimentally detect the SF state at low temperatures below T_c, whereas it may be difficult to probe the staggered current pattern in the zero-field uniform SC state because of spatial and temporal fluctuations. Possible experimental tests of the SF core were proposed as summarized below.[27] (1) Cyclotron resonance or Shubnikov-de Haas experiments in a high-quality underdoped sample at $H>H_{c2}$ can detect the small Fermi pockets around $(\pm\pi/2, \pm\pi/2)$ points with non-uniformly spaced Landau levels. (2) Muon-spin resonance or neutron-scattering experiments can directly detect the staggered currents that produce a small staggered magnetic field of order 10 G.[28] Intensity of the signal may increase upon increasing H, since the increasing H excites more vortices with the core size being independent of H. (3) Nuclear magnetic resonance (NMR) experiments can detect sidebands in the Y NMR line in $Y_2Ba_4Cu_7O_{15}$ samples with a splitting independent of H but with weight proportional to H. For this purpose, $Y_2Ba_4Cu_7O_{15}$ may be ideal because there are asymmetric bilayers where the Y ion sits in between, and it may be possible to have one plane of the bilayer optimally doped while the other plane (next to the double chain) remains underdoped, i.e., the staggered magnetic field at the Y site does not cancel.

Now we are naturally led to the following question: is it possible to detect a signature of the unit-cell doubling associated with the SF core through the state-of-the-art STM technique? It turned out that there is no effect inside the SF core, because what is staggering in the SF state is the currents, which does not show up in the charge density. This situation motivated us to look at the region outside the core. We addressed this problem in our previous paper[29] and found that whereas the center in the vortex core is a SF state, as one moves away from the core center, a correlated staggered modulation of the hopping amplitude χ_{ij} and pairing amplitude Δ_{ij} of the *physical* electrons becomes predominant. We predicted that in this region, the local density of states (LDOS) exhibits staggered modulation when measured on the bonds, which may be directly detected by STM experiments.

In this paper, we give a full account of the results summarized in Ref. 29 and examine the LDOS around the SU(2) vortex in detail. The outline is as follows. In Sec. II, we will give an overview of the SU(2) lattice-gauge-theory formulation of the t-J model (Sec. II A) and then discuss the topological texture of the SU(2) boson condensate based on the O(4) σ model (Sec. II B). We are mainly concerned with the LDOS outside the core through which we detect the unit-cell doubling stabilized by the robust topological texture. For this purpose, a close study of the vortex-core state is not necessary. To take account of the phase winding, we will apply a simple London model for a single vortex to the SU(2) vortex model (Sec. II C). In Sec. III, we discuss the hopping and pairing order parameters of the *physical* electron around the vortex. For this purpose, we perform an appropriate local SU(2) gauge transformation (Sec. III A). Then, we argue in detail that as one moves away from the core center, a correlated staggered modulation of χ_{ij} and Δ_{ij} becomes predominant (Sec. III B). In Sec. IV, we evaluate the LDOS outside the core. Formulation of the LDOS at an arbitrary point on the lattice is given in Sec. IV A. It is demonstrated that the LDOS exhibits a conspicuous staggered pattern only when measured on the bonds. To obtain the LDOS, we compute the lattice propagator by using two complementary approaches, which are presented in Secs. IV B and IV C. Finally, concluding remarks are given in Sec. V.

II. SU(2) VORTEX WITH THE STAGGERED FLUX CORE

In this section, we recapitulate the SU(2) lattice-gauge-theory formulation of the t-J model and then discuss the SU(2) vortex model in some detail.

A. SU(2) lattice-gauge-theory formulation of the t-J model

The t-J model Hamiltonian is given by

$$H=-t\sum_{\langle i,j\rangle,\sigma}(c_{i\sigma}^{\dagger}c_{j\sigma}+\text{H.c.})+J\sum_{\langle i,j\rangle}(\mathbf{S}_i\cdot\mathbf{S}_j-\tfrac{1}{4}n_in_j), \tag{2.1}$$

where $c_{i\sigma}^{\dagger}$ and $c_{i\sigma}$ are the projected electron operators with the constraint $n_i\leqslant 1$. In the SU(2) slave-boson approach,[12,13] a physical electron is represented as an SU(2) singlet formed out of the ''isospin'' doublets of the fermion $(\psi_{i\sigma})$ and boson (h_i),

$$c_{i\sigma}=\frac{1}{\sqrt{2}}h_i^{\dagger}\psi_{i\sigma}=\frac{1}{\sqrt{2}}(b_{i1}^{\dagger}f_{i\sigma}+\epsilon_{\sigma\bar{\sigma}}b_{i2}^{\dagger}f_{i\bar{\sigma}}^{\dagger}) \tag{2.2}$$

with

$$\psi_{i\sigma}=\begin{pmatrix} f_{i\sigma} \\ \epsilon_{\sigma\bar{\sigma}} f^{\dagger}_{i\bar{\sigma}} \end{pmatrix}, \quad h_i=\begin{pmatrix} b_{i1} \\ b_{i2} \end{pmatrix}. \tag{2.3}$$

The physical hole density $\langle b^{\dagger}_{i1}b_{i1}+b^{\dagger}_{i2}b_{i2}\rangle = x$ is enforced by the chemical potential μ. We need to introduce the temporal component of the gauge field $\mathbf{a}_{0i}$ to ensure the projection of the Hilbert space onto the SU(2) singlet subspace $(\frac{1}{2}\psi^{\dagger}_{i\sigma}\boldsymbol{\tau}\psi_{i\sigma}+h^{\dagger}_i\boldsymbol{\tau}h_i)|\mathrm{Phys}\rangle=0$, which is identical to that of the original t-J model. The conventional U(1) slave boson b_i is now regarded as the SU(2) boson doublet having only its isospin "up" component: $(h^{(0)}_i)^T=(b_i,0)$. The spin-liquid state is characterized by the order parameters $\Delta_{ij}=\langle \epsilon_{\sigma\sigma}f_{i\sigma}f_{j,\bar{\sigma}}\rangle$ and $\chi_{ij}=\langle f^{\dagger}_{i\sigma}f_{j\sigma}\rangle$, which constitute a 2×2 matrix

$$U_{ij}=\begin{pmatrix} -\chi^{*}_{ij} & \Delta_{ij} \\ \Delta^{*}_{ij} & \chi_{ij} \end{pmatrix}. \tag{2.4}$$

By this decoupling, the spin-exchange term is replaced with $\mathbf{S}_i\cdot\mathbf{S}_j \rightarrow (3J/16)\Sigma_{\sigma}\psi^{\dagger}_{i\sigma}U_{ij}\psi_{j\sigma}+(3J/16)\mathrm{Tr}[U^{\dagger}_{ij}U_{ij}]$. We should stress here that in the presence of the b_2 boson, χ_{ij} and Δ_{ij} cannot be interpreted as the hopping and pairing order parameters of a *physical electron* [see Eq. (2.2)]. The "phase" of U_{ij} is now interpreted as the SU(2) lattice-gauge fields:[8,30]

$$\overline{U}_{ij}=U_{ij}\exp[-i\mathbf{a}_{ij}\cdot\boldsymbol{\tau}], \tag{2.5}$$

where $\boldsymbol{\tau}=(\tau^1,\tau^2,\tau^3)$ are Pauli matrices and $\mathbf{a}_{ij}=(a^1_{ij},a^2_{ij},a^3_{ij})$ is the gauge field on every link. Now the t-J model is described by the fermion-boson system interacting with the SU(2) lattice-gauge field[12,13] described by the Lagrangian: $L_0=L^F_0+L^B_0+(\tilde{J}/2)\Sigma_{\langle ij\rangle}\mathrm{Tr}[\overline{U}^{\dagger}_{ij}\overline{U}_{ij}]$ with

$$L^F_0=\tfrac{1}{2}\sum_{i,j,\sigma}\psi^{\dagger}_{i\sigma}[\delta_{ij}\partial_{\tau}+\tilde{J}\overline{U}_{ij}]\psi_{j\sigma}+\tfrac{1}{2}\sum_{i,\sigma}\psi^{\dagger}_{i\sigma}i\mathbf{a}_{0i}\cdot\boldsymbol{\tau}\psi_{i\sigma}, \tag{2.6}$$

$$L^B_0=\sum_{i,j}h^{\dagger}_i[\delta_{ij}(\partial_{\tau}-\mu)+\tilde{t}\overline{U}_{ij}]h_j+\sum_i h^{\dagger}_i i\mathbf{a}_{0i}\cdot\boldsymbol{\tau}h_i, \tag{2.7}$$

where $\tilde{J}=3J/8$ and $\tilde{t}=t/2$. The mean-field solution is obtained by integrating out the fermions and minimizing the mean-field energy $E(\{U_{ij},h_i\})$, which leads to U_{ij} on the links and the boson h_i on the sites.

The SU(2) gauge invariance is realized through the relation $E(\{\overline{U}_{ij},h_i\})=E(\{W_i\overline{U}_{ij}W^{\dagger}_j,W_ih_i\})$ for any $W_i\in\mathrm{SU}(2)$. Thanks to the SU(2) symmetry, we can choose a convenient gauge fixing to describe the MF state in an SU(2) invariant way. Convenient gauge choices in the underdoped regime are the "d-wave gauge" or the "staggered-flux (SF) gauge" specified by

$$U^d_{ij}=-\chi_0\tau^3+(-1)^{i_y+j_y}\Delta_0\tau^1, \tag{2.8}$$

$$U^{\mathrm{SF}}_{ij}=-A\tau^3\exp[i(-1)^{i_x+j_y}\Phi_0\tau^3], \tag{2.9}$$

respectively, where $A=\sqrt{\chi^2_0+\Delta^2_0}$ and $\Phi_0=\tan^{-1}(\Delta_0/\chi_0)$. Equation (2.8) describes fermions with d-wave pairing order parameters, while Eq. (2.9) describes fermion hopping with flux $\pm 4\Phi_0$ on alternating plaquetts.[2] At zero doping ($x=0$) there is no boson and these apparently different mean-field *Ansätze* describe exactly the same MF state, since U^d_{ij} and U^{SF}_{ij} are just SU(2) gauge equivalent, i.e., $U^d_{ij}=w_iU^{\mathrm{SF}}_{ij}w^{\dagger}_j$ $[E(\{U^d_{ij}\})=E(\{w_iU^{\mathrm{SF}}_{ij}w^{\dagger}_j\})=E(\{U^{\mathrm{SF}}_{ij}\})]$, where the transformation is explicitly given by

$$w_i=\exp\left[i(-1)^{i_x+i_y}\frac{\pi}{4}\tau^1\right]. \tag{2.10}$$

Upon doping, however, the U^d_{ij} with the U(1) boson condensate $(h_{0i})^T=(b_i,0)=(\sqrt{x},0)$ characterizes the physical d-wave SC state, while the U^{SF}_{ij} with the U(1) boson condensate $(h_{0i})^T=(\sqrt{x},0)$ characterizes the physical SF state. These states are no longer physically equivalent because of the presence of the boson condensate $[E(\{U^d_{ij},h_{0i}\})\neq E(\{U^{\mathrm{SF}}_{ij},h_{0i}\})]$ and the SC phase is picked out as the MF solution.[9,10] Accordingly, the "flux" $\Phi_0=\tan^{-1}(\Delta_0/\chi_0)$ decreases from $\Phi_0=\pi/4$ (π-flux phase) upon doping.[9,10]

The advantage of the SF gauge is that it is apparent that the SU(2) symmetry has been broken down to the residual U(1), which we denote as $\mathrm{U(1)_{res}}$ since U^{SF}_{ij} contains only τ^3.[31] The lattice-gauge fields a^1_{ij} and a^2_{ij} become massive by the Anderson-Higgs mechanism and can be ignored, while a^3_{ij} remains massless and is the important low-energy degree of freedom that should be included, i.e., we consider

$$\overline{U}^{\mathrm{SF}}_{ij}=-A\tau^3\exp[i(-1)^{i_x+j_y}\Phi_0\tau^3]\exp[-ia^3_{ij}\tau^3]. \tag{2.11}$$

In this gauge, we can discuss a vortex structure under the external magnetic field in a way quite similar to the conventional BCS vortex where the gauge structure is characterized by only the electromagnetic (EM) $\mathrm{U(1)_{EM}}$. The difference is that, in our problem, the gauge structure is characterized by $\mathrm{U(1)_{EM}}\otimes\mathrm{U(1)_{res}}$.

B. O (4) σ-model description of the local boson condensate

In the presence of a magnetic field, the mean-field solution contains vortices. The SU(2) vortex model[27] was discussed based on the O(4) σ-model description for a slowly varying boson condensate.[13] The basic idea is that at low temperatures the bosons are nearly condensed to the bottom of the band and are slowly varying in space and time. The *Ansätze* (2.8) and (2.9) gives the one-boson dispersion $\xi^B_k=-\tilde{t}A(\cos^2k_x+\cos^2k_y+2\cos 2\Phi_0\cos k_x\cos k_y)^{1/2}$. The b_1 and b_2 bosons are then nearly condensed to the band bottom (0, 0) and (π,π), respectively.[32] On the other hand, the fermions are fluctuating over the lattice scale and can be integrated out, after choosing an $\mathbf{a}_{0i}$ field, which minimize the action locally. This view is in the spirit of the Born-Oppenheimer approximation.[13] In the SF gauge given by Eq. (2.9), the local boson condensate (LBC) can be written as

$$\overline{h}_i^{\mathrm{SF}} = \sqrt{x}\begin{pmatrix} z_{i1} \\ -i(-1)^{i_x+i_y} z_{i2} \end{pmatrix}, \tag{2.12}$$

where z_{i1} and z_{i2} [CP^1 fields] are slowly varying in space and time and are parametrized by

$$z_{i1} = e^{i\varphi_{1i}} \cos\frac{\theta_i}{2}, \quad z_{i2} = e^{i\varphi_{2i}} \sin\frac{\theta_i}{2}, \tag{2.13}$$

with the internal phases being given by

$$\varphi_{1i} = \alpha_i - \phi_i/2, \quad \varphi_{2i} = \alpha_i + \phi_i/2. \tag{2.14}$$

We shall give some remarks on the expression Eq. (2.12) in Appendix A.

The overall phase angle α is associated with the $\mathrm{U(1)}_{\mathrm{EM}}$. The internal SU(2) gauge symmetry is broken down to $\mathrm{U(1)}_{\mathrm{res}}$ and the angles ϕ and θ are interpreted as polar angles of the manifold of the LBC: $\mathrm{SU(2)/U(1)}_{\mathrm{res}} \simeq S^2$. Topological stability of vortex formation is indicated by the nontrivial topology, $\pi_2[\mathrm{SU(2)/U(1)}_{\mathrm{res}}] = \pi_1[\mathrm{U(1)}_{\mathrm{res}}] = \mathbf{Z}$. The internal degrees of freedom of the LBC is visualized by the vector

$$\mathbf{I}_i = z_i^\dagger \boldsymbol{\tau} z_i = (\sin\theta_i \cos\phi_i, \sin\theta_i \sin\phi_i, \cos\theta_i), \tag{2.15}$$

which has the meaning of the quantization axis for the z fields, $(z_i)^T = (z_{i1}, z_{i2})$. In the SF gauge, the uniform d-wave SC state and the uniform SF state are described by $\theta_i = \pi/2$ and $\theta_i = 0$, π, respectively. The angle ϕ_i is associated with the residual gauge symmetry $\mathrm{U(1)}_{\mathrm{res}}$, which is further broken down to $\{\mathbf{0}\}$ upon Bose condensation, which triggers the superconducting phase transition.

The low-energy dynamics of the LBC is described by an anisotropic O(4) σ model coupled to the gauge fields.[13] Since we are only concerned with static configurations, we shall ignore the time-dependent terms from now on. The free energy associated with this model is written in a form $F_{\mathrm{eff}} = F_K + F_\perp + F_A + F_a$ explained below. In the SU(2) formulation, only the boson can carry charge. Under the magnetic field, the boson hopping-pairing matrix in Eq. (2.7) acquires an EM Peierls phase,

$$\overline{U}_{ij}^{\mathrm{SF}} \to \overline{U}_{ij}^{\mathrm{SF}} \exp\left[i\tfrac{e}{c} \int_{\mathbf{r}_i}^{\mathbf{r}_j} \mathbf{A}(\mathbf{r}) \cdot d\mathbf{r} \right]$$

Taking a continuum limit, the kinetic part is written as

$$F_K = \frac{x}{2m_b} \int d\mathbf{r} |\boldsymbol{\mathcal{D}} z|^2, \tag{2.16}$$

where we introduced the boson mass $m_b \sim 1/t$. The covariant derivative is given by $\boldsymbol{\mathcal{D}} = \boldsymbol{\nabla} + i\mathbf{a}^3\tau^3 - i\frac{e}{c}\mathbf{A}$, where we introduced the continuum limit of the a_{ij}^3 field through $a_{ij}^3 = (\mathbf{r}_i - \mathbf{r}_j) \cdot \mathbf{a}^3(\mathbf{r}_i/2 + \mathbf{r}_j/2)$.

The anisotropy term is phenomenologically given in a form

$$F_\perp = \frac{x^2\tilde{J}}{2} \int d\mathbf{r} \left[\frac{4}{c_1} |z_1 z_2|^2 + \frac{1}{c_3} (|z_1|^2 - |z_2|^2)^2 \right], \tag{2.17}$$

with c_1 and c_3 being numerical constants of the order of unity.[13] This term describes energy cost associated with small fluctuations of the LBC around the SC state ($\theta = \pi/2$). For $c_3 < c_1$, the **I** vector prefers to lie in the τ_1-τ_2 plane (equatorial plane) and the SC state is favored.

The conventional EM Maxwell term is given by

$$F_A = \frac{1}{8\pi} \int d\mathbf{r} (\boldsymbol{\nabla} \times \mathbf{A})^2. \tag{2.18}$$

The fourth term F_a, the internal gauge-field kinetic term, is dynamically induced by integrating out the fermion degrees of freedom although we have no such term initially at the relevant highest-energy scales of the fermions $\sim \chi_0 J$. We have

$$F_a = \frac{\sigma}{2} \sum_{\mathbf{q}} \sum_{\mu,\nu=x,y} a_\mu^3(\mathbf{q}) \Pi_{\mu\nu}^F(\mathbf{q}) a_\nu^3(\mathbf{q}), \tag{2.19}$$

where $\sigma = \sqrt{\tilde{J}\Delta}$ and the fermion polarization bubble originating from the coupling term of the Dirac fermion current and gauge field is given by

$$\Pi_{\mu\nu}^F(\mathbf{q}) = \left(\delta_{\mu\nu} - \frac{q_\mu q_\nu}{q^2} \right) |\mathbf{q}|. \tag{2.20}$$

We note that this does not take the EM Maxwell form which is proportional to $\mathbf{q}^2$ and which consequently gives rise to a nonlocal kernel in real space,

$$F_a = \frac{\sigma}{2} \int d\mathbf{r} \int d\mathbf{r}' \kappa(\mathbf{r} - \mathbf{r}') \mathbf{h}(\mathbf{r}) \cdot \mathbf{h}(\mathbf{r}'). \tag{2.21}$$

where $\mathbf{h}(\mathbf{r}) = \boldsymbol{\nabla} \times \mathbf{a}^3(\mathbf{r})$ and $\kappa(\mathbf{r} - \mathbf{r}') = \Sigma_{\mathbf{q}} e^{-i\mathbf{q}\cdot(\mathbf{r}-\mathbf{r}')} \kappa_{\mathbf{q}}$ with

$$\kappa_{\mathbf{q}} = 1/|\mathbf{q}|, \tag{2.22}$$

instead of $\kappa_{\mathbf{q}} = 1$ in case of the conventional EM kernel.

C. London model of a single SU(2) vortex

In the model of the vortex proposed by Lee and Wen, both α and $\phi/2$ wind by π and consequently give an appropriate $hc/2e$ vortex for the EM gauge field $\mathbf{A}(\mathbf{r})$. This way of winding is specified by

$$\boldsymbol{\nabla}\alpha = \boldsymbol{\nabla}\frac{\phi}{2} = \frac{\hat{\mathbf{e}}_\phi}{2r}, \tag{2.23}$$

which lead to $\boldsymbol{\nabla}\varphi_1 = 0$ and $\boldsymbol{\nabla}\varphi_2 = \hat{\mathbf{e}}_\phi/r$, where $\hat{\mathbf{e}}_\phi$ denotes the azimuthal unit vector in the physical space. That is to say, only b_2 changes its phase φ_2 by 2π as we go around the vortex, while b_1 does not.

The texture of the **I** vector in the SF gauge is indicated in Fig. 1(a). In the SC state outside the core, $\mathbf{I}_i = (\cos\phi_i, \sin\phi_i, 0)$, while as we approach the core, $|b_2|$ must vanish and the vortex center is represented by $\mathbf{I}_i = (0,0,1)$, which is just the SF state. The $\mathbf{I}_i$ vector tilts smoothly from the equator to the north pole as the core is approached with a length scale denoted by l_c, which is identified with the core size. To determine the SU(2) vortex structure, we shall use the ''London-model'' prescription of a single vortex in ex-

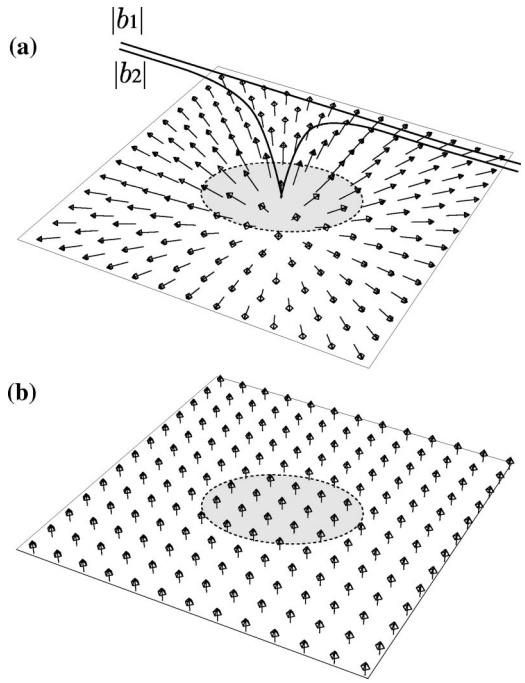

FIG. 1. (a) The texture of the **I** vector in the SU(2) vortex configuration in the SF gauge. At the center of the vortex, $\mathbf{I}_i$ points toward the north pole corresponding to the SF state. The shaded circle depicts the vortex core. The local gauge transformation g_i transforms this configuration to (b) in the *d*-wave gauge, where the internal phases of the bose condensate are gauged away.

treme type-II BCS superconductor.[33] A detailed account of the analysis is given in Appendix B.

Although quantitative estimation of l_c and λ_a is beyond the present simple London-model analysis, l_c presumably extends over a fermion coherence length $\xi_F \sim v_F/\Delta$, which may amount to a few lattice scales as suggested numerically.[25] We here just remark that there are two kinds of vortices, because the **I** vector can also point toward the south pole at the vortex core: $\theta_i = \pi$ in Eq. (2.13). This just expresses the state with the staggered flux shifted by one unit cell. If the center of the vortex is in the center of the plaquette, the degeneracy between these two kinds of vortices is broken by the circulation of the EM superfluid current. This is the situation considered by Wang, Han, and Lee[26] in their numerical local U(1) mean-field approach. On the other hand, if the center of the vortex is on a lattice site, the degeneracy remains and there is quantum-mechanical tunneling between the two states. The tunneling rate depends on l_c and is difficult to estimate. However, the dissipation due to quasiparticles may suppress the tunneling rate due to the *orthogonality catastrophe*. Whether the two states are degenerate or not depends on short-distance physics, which is outside the domain of our long-wavelength theory.

III. HOPPING AND PAIRING ORDER PARAMETERS OF THE PHYSICAL ELECTRONS AROUND A SINGLE VORTEX

A. Gauge transformation of the local boson condensate

Now that the SU(2) vortex model has been established, we shall discuss the effects of the unit-cell doubling and the phase winding on the hopping and pairing order parameters of the *physical* electrons around a single vortex. For this purpose, it is best to work with the *d*-wave gauge after making a local gauge transformation

$$g_i = \exp\left[i(-1)^{i_x+i_y} \frac{\theta_i}{2} \tau^1 \right] \exp\left[i \frac{\phi_i}{2} \tau^3 \right]. \tag{3.1}$$

The LBC is then transformed to

$$\overline{h}^{\mathrm{SF}} \to \overline{h}_i^d = g_i \overline{h}_i^{\mathrm{SF}} = e^{i\alpha_i} \begin{pmatrix} \sqrt{x} \\ 0 \end{pmatrix}, \tag{3.2}$$

i.e., the **I** vector points toward the north pole *everywhere on the lattice*, as shown in Fig. 1(b). We here consider only the case of a single vortex. The great advantage of the *d*-wave gauge is that the physical electron operator is simply written as

$$c_{i\sigma} = \frac{1}{\sqrt{2}} \overline{h}_i^{d\dagger} \psi_{i\sigma} = e^{-i\alpha_i} \sqrt{x/2} f_{i\sigma}, \tag{3.3}$$

i.e., the fermions behave as physical electron. After the local gauge transformation to the *d*-wave gauge, we find

$$\begin{aligned} \overline{U}_{ij}^{\mathrm{SF}} \to \overline{U}_{ij}^d = g_i \overline{U}_{ij}^{\mathrm{SF}} g_j^\dagger = & -\tilde{\chi}_{ij} \left[\tau^3 \cos\frac{\theta_i - \theta_j}{2} \right. \\ & \left. + (-1)^{i_x+i_y} \tau^2 \sin\frac{\theta_i - \theta_j}{2} \right] \\ & - \tilde{\Delta}_{ij} \left[i(-1)^{i_x+j_y} \cos\frac{\theta_i + \theta_j}{2} \right. \\ & \left. - (-1)^{i_y+j_y} \tau^1 \sin\frac{\theta_i + \theta_j}{2} \right], \end{aligned} \tag{3.4}$$

where

$$\tilde{\chi}_{ij} = A \cos\Phi_{ij}, \quad \tilde{\Delta}_{ij} = A \sin\Phi_{ij}, \tag{3.5}$$

$$\Phi_{ij} = \Phi_0 + (-1)^{i_x+j_y} v_{ij}, \tag{3.6}$$

and

$$v_{ij} = \frac{\phi_i - \phi_j}{2} - a_{ij}^3. \tag{3.7}$$

As an important consequence of the local gauge transformation, the gauge-invariant quantity v_{ij} enters Eq. (3.4). The quantity has a meaning of the fermion "superfluid velocity" associated with the internal gauge field $\mathbf{a}^3$, which is circulating around the vortex center [see Eq. (B4)]. For example, let us consider $v_y(\mathbf{r})$ along the line $i_y = \frac{1}{2}$, assuming that the vortex center sits at $(\frac{1}{2}, \frac{1}{2})$. The Fourier transform of Eq. (B10) gives

$$v_y(\mathbf{r}) = \frac{1}{2r} - \frac{1}{2} \int_0^\infty dq \, \frac{J_1(q i_x)}{1 + \lambda_a q}, \tag{3.8}$$

where $\mathbf{r} = (i_x, \frac{1}{2})$. In Fig. 2, we show the spatial distribution of $v_y(\mathbf{r})$ by assuming the gauge field-penetration depth to be

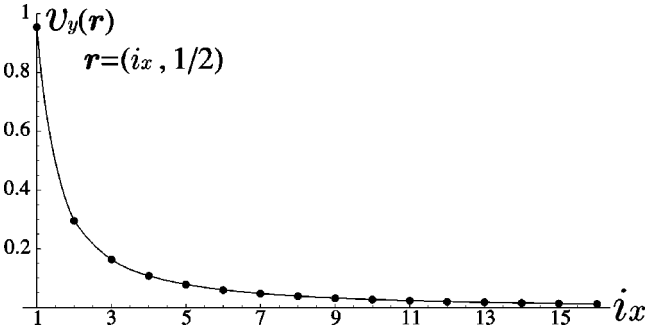

FIG. 2. Spatial distribution of the superfluid velocity $v_y(\mathbf{r})$ associated with the internal gauge field $\mathbf{a}^3$. We assumed the gauge field-penetration depth to be $\lambda_a=10$ with the lattice unit. The origin should not be taken too literally, since $\mathbf{v}$ is defined in the continuum limit.

$\lambda_a=10$ with lattice unit. We see that $v_y(\mathbf{r})$ decays over the length scale λ_a, as is naturally expected for the superfluid velocity.

Let us write $\overline{U}^d_{ij}$ in the form

$$\overline{U}^d_{ij}=\begin{pmatrix} -\overline{\chi}^*_{ij} & \overline{\Delta}_{ij} \\ \overline{\Delta}^*_j & \overline{\chi}_{ij} \end{pmatrix}. \tag{3.9}$$

An essential point is that in the *d*-wave gauge $\overline{\chi}_{ij}$ *and* $\overline{\Delta}_{ij}$ *have the meaning of the hopping and pairing order parameters of the physical electron*, since the physical electron operator $c_{i\sigma}$ is just proportional to the auxiliary fermion operator $f_{i\sigma}$ [Eq. (3.3)]. Below we discuss the meaning of $\overline{\chi}_{ij}$ and $\overline{\Delta}_{ij}$ at different limits.

B. Hopping-pairing order parameters in the vicinity and outside of the vortex core

1. Vicinity of the vortex center

First, we consider the vicinity of the vortex center, where $\theta_i\sim\theta_j\sim 0$ and Eq. (3.9) becomes

$$\overline{U}^d_{ij}\sim -A\tau^3\exp[i(-1)^{i_x+i_y}\Phi_{ij}\tau^3], \tag{3.10}$$

i.e.,

$$\overline{\chi}_{ij}=A\exp[i(-1)^{i_x+j_y}\Phi_{ij}], \tag{3.11}$$

$$\overline{\Delta}_{ij}=0. \tag{3.12}$$

Equation (3.12) indicates that the superconducting order parameter is killed at the vortex center. In this region, as is directly seen from Eq. (3.11), what is modulated is the phase of the fermion hopping parameter, which is just regarded as the electron-hopping parameter. We see that the sum of the phase around an elementary plaquette yields modulated net flux $\pm 4\Phi_0+\phi_{\text{gauge}}(r)$ with $\pm$signs alternating from plaquette to plaquette. We here introduced a gauge flux penetrating an elementary plaquette centered at $\mathbf{r}\neq 0$,

$$\phi_{\text{gauge}}(r)=\oint_{\square}\boldsymbol{\nabla}\times\boldsymbol{v}\cdot d\mathbf{l}\sim\frac{c_0^2}{\hbar}h(r), \tag{3.13}$$

where we retained the lattice constant c_0. The internal gauge-field strength $\mathbf{h}(r)=\boldsymbol{\nabla}\times\mathbf{a}^3$ is given by Eq. (B8). We see $\phi_{\text{gauge}}(r)\ll 4\Phi_0\sim O(1)$ [for example, $\phi(2c_0)=0.03$ if we take $\lambda_a=10c_0$]. This situation just indicates the fact that the net flux is dominated by the original staggered flux $4\Phi_0$. Thus, inside the core the staggered phase modulation becomes predominant: $\overline{U}^d_{ij}\sim -A\tau^3\exp[i(-1)^{i_x+j_y}\Phi_0\tau^3]$.

The $\overline{U}^d_{ij}$ then breaks not only the translational symmetry ($\overline{U}^d_{ij}\neq\overline{U}^d_{i+\hat{\mathbf{e}}_\mu,j+\hat{\mathbf{e}}_\nu}$, where $\hat{\mathbf{e}}_\mu$ with μ, $\nu=x,y$ denotes a unit vector connecting the neighboring sites), but also the time-reversal symmetry with respect to the local bonds ($\overline{U}^d_{ij}\neq[\overline{U}^d_{ij}]^*$). Although we cannot explicitly analyze the electronic states inside the core, the time-reversal symmetry breaking implies that the staggered fermion currents flow on the bonds just as in the case of a uniform SF state. Once the bosons are condensed, the currents come up as the staggered orbital currents of the physical hole.[27]

In this paper, we are concerned with the possibility of detecting a signature of the unit-cell doubling through STM measurement. We immediately see that there is no hope in the SF state, because what is staggering in the SF phase is the on-bond currents caused by the staggered phase [Eq. (3.11)]. Consequently, the period doubling of the current never shows up in the LDOS.[35] This situation motivates us to look at the region outside the core.

2. Outside the SF core

We consider the region outside the SF core. We approximately set $\theta_i\sim\theta_j\sim\pi/2$, which gives

$$\overline{U}^d_{ij}\sim -\tilde{\chi}_{ij}\tau^3+(-1)^{i_y+j_y}\tilde{\Delta}_{ij}\tau^1, \tag{3.14}$$

i.e.,

$$\overline{\chi}_{ij}=\tilde{\chi}_{ij}, \tag{3.15}$$

$$\overline{\Delta}_{ij}=\tilde{\Delta}_{ij}. \tag{3.16}$$

Recalling that $\overline{\chi}_{ij}$ and $\overline{\Delta}_{ij}$ are interpreted as the hopping and pairing amplitudes of physical electrons, we see that *the region outside the SF core and inside the gauge-field-penetration depth, $l_c\lesssim r\lesssim\lambda_a$ around the vortex, is characterized by the staggered modulation of the hopping and pairing amplitudes*. Note that the amplitude of $\overline{\chi}_{ij}$ and $\overline{\Delta}_{ij}$ are modulated in a correlated way according to Eq. (3.5) to preserve

$$\tilde{\chi}^2_{ij}+\tilde{\Delta}^2_{ij}=\text{const.} \tag{3.17}$$

In Fig. 3, we depict the situation given by Eqs. (3.5), (3.15), (3.16), and (3.17).

$\overline{U}^d_{ij}$ breaks the translational symmetry, but does not breaks the time-reversal symmetry with respect to the local bonds. Therefore, $\overline{U}^d_{ij}$ does not cause local fermion current on the bonds [of course, even in this case, the external magnetic

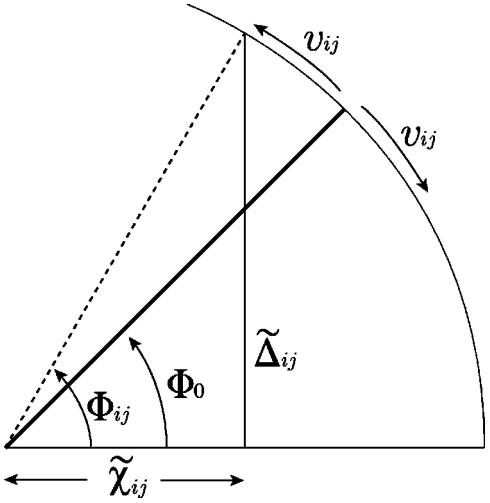

FIG. 3. Geometric relation of $\tilde{\chi}_{ij}$ and $\overline{\Delta}_{ij}$. The angle Φ_{ij} modulates around Φ_0 in a staggered manner [see Eq. (3.6)].

field breaks time-reversal symmetry and causes globally circulating supercurrent given by Eq. (B6)]. What is staggering in this region is not the local current but the local density on the bonds.

The temporal component of the gauge field, $\mathbf{a}^d_{0_i}$, is determined locally by the LBC. In the uniform case, the saddle point is purely imaginary. There, we can regard the LBC as almost uniform in the SC state outside the vortex core. Therefore it may be legitimate to assume $\mathbf{a}^d_{0i}$ to be uniform and parallel to the LBC (pointing toward the north pole) in this region [this assumption is reliable as far as deviation of θ_i from $\sim\pi/2$ is small]. From now on, we set

$$i\mathbf{a}^d_{0i}=(0,0,a_0), \tag{3.18}$$

where a_0 has an order of $x\tilde{J}$.

For the purpose of seeing a physical situation, we assume the SF core size to be $l_c=3$ and a simple distribution of the angle θ as indicated in Fig. 4(a). In Figs. 4(b) and 4(c), respectively, we show the corresponding spatial variation of $\tilde{\chi}_{ij}$ and $\tilde{\Delta}_{ij}$ on the link connecting $(i_x,0)$ and $(i_x,1)$ with the lattice unit. We also assumed the gauge-field-penetration depth to be $\lambda_a=10$. Now $\tilde{\Delta}_{ij}$ just represents pairing amplitude of the physical electron and vanishes at the vortex center as it should do. As we go away from the core, $\overline{\chi}_{ij}$ and $\overline{\Delta}_{ij}$ acquire staggered modulation with the amplitude becoming smaller, because the superfluid velocity $v(\mathbf{r})$, which is responsible for the appearance of the staggered modulation, becomes smaller. In fact, the staggered modulation of $\overline{\chi}_{ij}$ is just of an order of a few percent, while that of $\overline{\Delta}_{ij}$ is rather large. However, as we shall see shortly, *period doubling* caused by this modulation gives rise to visible effects in LDOS *outside the core*. We should also remark that both $\overline{\chi}_{ij}$ and $\overline{\Delta}_{ij}$ contribute to the LDOS. The problem now reduces to the more familiar U(1) mean-field theory, but with χ_{ij} and Δ_{ij}, which vary in space. This is precisely the problem treated by Han, Wang, and Lee[25,26] and it is gratifying that they found numerically the staggered current around the vortex core as proposed in the SU(2) vortex model.[27]

In Fig. 5, we schematically show the modulation pattern of $\overline{\chi}_{ij}$ outside the core. The staggered modulation becomes most conspicuous when scanned along the straight line $i_x=\frac{1}{2}$ or $i_y=\frac{1}{2}$, provided that the vortex center sits at $(\frac{1}{2},\frac{1}{2})$, because on these bonds the circulating $\mathbf{v}(\mathbf{r})$ field becomes parallel to the bond directions. Apparently, the bond-modulation pattern reminds us of the spin-Peierls states. However, this is not the case, since the MF expectation value of spin-exchange energy on the bonds is given by $\langle \mathbf{S}_i\cdot\mathbf{S}_j\rangle$

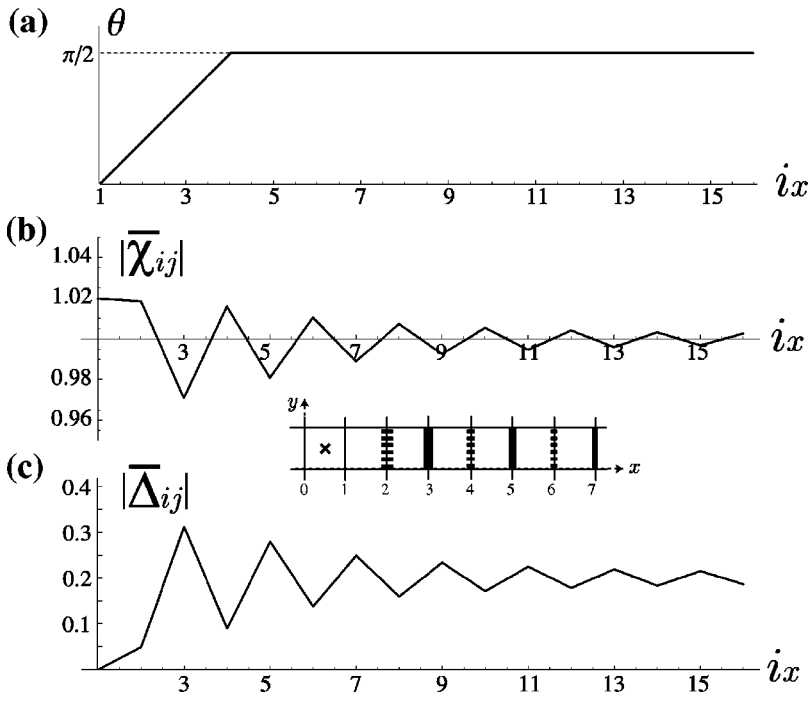

FIG. 4. A simple distribution of the θ indicated in (a) leads to spatial variation of (b) $\overline{\chi}_{ij}$ and (c) $\overline{\Delta}_{ij}$ on the link connecting $(i_x,0)$ and $(i_x,1)$ as indicated in the inset. The gauge-field-penetration depth is assumed to be $\lambda_a=10$.

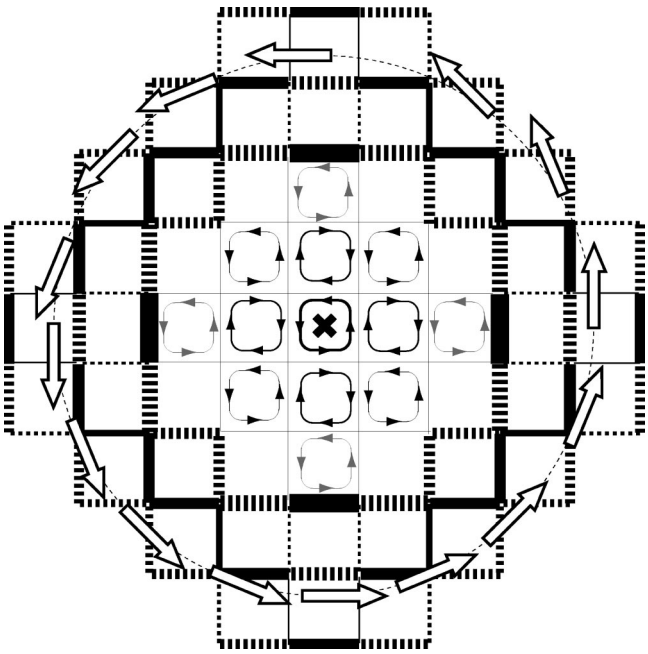

FIG. 5. Schematic drawing of the amplitude-modulation pattern of the hopping parameter $\tilde{\chi}_{ij}$ outside the SF core. Solid and dotted bonds indicate enhanced and reduced amplitudes, respectively, where thickness of the bonds qualitatively represents magnitude of the modulation. Circulation of the the fermion ''superfluid velocity'' $\mathbf{v}(\mathbf{r})$ associated with the internal gauge field $\mathbf{a}^3$ is indicated by the arrows. The staggered modulation becomes most conspicuous when scanned along the lines $i_x=\frac{1}{2}$ or $i_y=\frac{1}{2}$, provided that the vortex center sits at $(\frac{1}{2},\frac{1}{2})$. Note that the boundary of the SF core region, inside which the staggered orbital currents flow, should not be taken literally. In reality, there is a crossover region around $r\sim l_c$ where the staggered current and the staggered amplitude modulation coexists.

$=-\tilde{J}(\overline{\chi}_{ij}^2+\overline{\Delta}_{ij}^2)=$const and therefore the spin-Peierls order parameter becomes $\langle \mathbf{S}_i\cdot\mathbf{S}_{i+\hat{\mathbf{e}}_\mu}-\mathbf{S}_i\cdot\mathbf{S}_{i-\hat{\mathbf{e}}_\mu}\rangle=0$ with $\hat{\mathbf{e}}_\mu$ being a unit vector connecting the neighboring sites.

As we approach the core from the outside, the **I** vector in the SF gauge gradually rises off from the equatorial plane [see Fig. 1(a)]. This may give rise to a crossover region characterized by coexistence of the amplitude and phase modulation, where θ dependence of $\overline{U}_{ij}^d$ becomes significant. It is expected that the staggered current begins to appear around $r\sim l_c$ and its strength becomes stronger as we approach the immediate center of the vortex. We give a schematic drawing of this circumstance in Fig. 5. To study the effects of θ-dependent $\overline{U}_{ij}^d$ is, however, beyond the scope of the present paper and we concentrate on the region $l_c\lesssim r\lesssim\lambda_a$. We should also remark that when the angle θ deviates from $\theta_i=\theta_j=\pi/2$ as we approach the core, the direction $\mathbf{a}_{0i}^d$ begins to slightly deviate from the north pole, since $\mathbf{a}_{0i}^d$ is no longer parallel to the **I** vector due to small anisotropy. In the next section, we shall compute the LDOS in the SC state outside the core by setting $\theta_i=\theta_j=\pi/2$. Then, $\mathbf{a}_{0i}^d$ is given by Eq. (3.18) and is exactly parallel to the **I** vector pointing toward the north pole. We expect our results to be qualitatively valid even for $r\sim l_c$ as long as we avoid the inside of the core.

IV. LDOS OUTSIDE THE CORE

As we saw in the preceding section, the staggered modulation of the hopping amplitude $\overline{\chi}_{ij}$ and pairing amplitude $\overline{\Delta}_{ij}$ becomes predominant over the region $l_c\lesssim r\lesssim\lambda_a$. The presence of staggered modulation suggests that this may be the best place to look for the unit-cell-doubling effect. In this section, we consider the LDOS in this region.

A. Formulation of LDOS

The local density of states at an arbitrary point **r** on lattice is defined by

$$N(\mathbf{r},\omega)=-\frac{2}{\pi}\mathrm{Im}\mathcal{G}^{\mathrm{phys}}(\mathbf{r},\mathbf{r};i\omega)|_{i\omega\to\omega+i\delta}, \tag{4.1}$$

where the propagator for the physical electron is introduced by $\mathcal{G}^{\mathrm{phys}}(\mathbf{r},\mathbf{r}',i\omega)=-\int_0^\beta d\tau\, e^{i\omega\tau}\ \langle T_\tau c_\sigma(\mathbf{r},\tau)c_\sigma^\dagger(\mathbf{r}')\rangle$. To model the tunneling current we assume that the electron tunnel from the tip located at **r** to a linear combination of Wannier orbitals centered at lattice sites, i.e., the physical electron operator at $\mathbf{r}, c_\sigma(\mathbf{r})$, is related to $c_{i\sigma}$ as

$$c_\sigma(\mathbf{r})=\sum_i\ \alpha_i(\mathbf{r})\exp\left[-i\tfrac{e}{c}\int_{\mathbf{r}_i}^{\mathbf{r}}d\mathbf{r}'\cdot\mathbf{A}(\mathbf{r}')\right]c_{i\sigma}, \tag{4.2}$$

where the EM gauge potential **A** gives rise to the EM Peierls phase. The envelope function $\alpha_i(\mathbf{r})$ may be simulated by $\alpha_i(\mathbf{r})=e^{-|\mathbf{r}-\mathbf{r}_i|/\xi}$ in the bond direction (the Cu-O-Cu bond). The length scale ξ can reasonably be set equal to $\xi=\frac{1}{2}$ with the lattice scale corresponding to the Cu-O separation. Since the effects of the EM gauge fields are negligibly small in strength as compared with the internal gauge potential, from now on, we ignore the EM Peierls phase and examine the effects of the staggered hopping and pairing amplitudes on the LDOS. Noting Eq. (3.3) in the *d*-wave gauge, Eq. (4.1) is written as

$$N(\mathbf{r},\omega)=-\frac{x}{\pi}\mathrm{Im}\sum_{i,j}\ \alpha_i(\mathbf{r})\alpha_j(\mathbf{r})[\mathcal{G}_{ij}^F(i\omega)]_{11}|_{i\omega\to\omega+i\delta}. \tag{4.3}$$

The subscript 11 means the 11 component of the lattice fermion propagator of a 2×2 matrix form, $\mathcal{G}_{ij}^F(\tau)=-\langle T_\tau\psi_{i\sigma}(\tau)\psi_{j\sigma}^\dagger\rangle$.

We here give an intuitive demonstration that the LDOS exhibits a conspicuous staggered pattern *only when measured on the bonds*. A more quantitative discussion will be given in the following sections. For example, we pick up the sites 1,2,...,6 indicated in Fig. 6 and consider the midpoints on the bonds B_1, B_2 and the plaquette centers C_1, C_2. The LDOS at C_1 and C_2 come from $\Sigma_{i,j=1,2,4,5}\mathcal{G}_{ij}^F$ and $\Sigma_{i,j=2,3,5,6}\mathcal{G}_{ij}^F$, respectively. We see, however, $\mathcal{G}_{12}^F\sim\mathcal{G}_{56}^F$ because the bonds 12 and 56 are almost equivalent except the effects of negligibly small dependence of the **v** field on the spatial position **r** over the lattice scales. Similarly, $\mathcal{G}_{45}^F\sim\mathcal{G}_{23}^F$ and $\mathcal{G}_{14}^F\sim\mathcal{G}_{36}^F$.

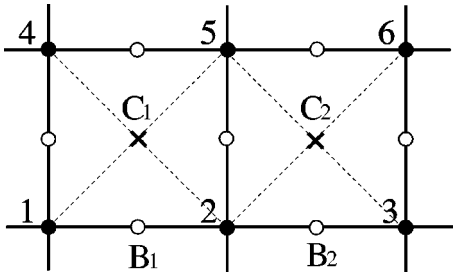

FIG. 6. Points on lattice where we consider the LDOS. We have four symmetrically distinct points: the plaquette center (×), site top (●), and bond center (○). The site-top and bond-center points correspond to the Cu and O sites, respectively.

Therefore, $N(\mathbf{r}_{C_1},\omega)\sim N(\mathbf{r}_{C_2},\omega)$. Similarly, the LDOS at the lattice sites is almost uniform. On the other hand, the LDOS at B_1 and B_2 come from $\Sigma_{i,j=1,2}\mathcal{G}^F_{ij}$, and $\Sigma_{i,j=2,3}\mathcal{G}^F_{ij}$, respectively. Here, $\mathcal{G}^F_{12}$ and $\mathcal{G}^F_{23}$ are clearly inequivalent because they connect the bonds with alternating hopping-pairing amplitudes.

To compute $\mathcal{G}^F_{ij}(i\omega)$ in the SC state outside the core, we shall use the following two approaches that may be complementary to each other: (i) a perturbative analysis using the gradient expansion and (ii) an exact diagonalization using the ''uniform **v**'' approximation. In the former approach, we can take account of the circulating configuration of the $v(\mathbf{r})$ field, while in the latter approach, instead, we can obtain a nonperturbative aspect of the problem.

B. Perturbative analysis using the gradient expansion

First, we expand Eq. (3.5) with respect to v_{ij} up to the first order as

$$\tilde{\chi}_{ij}\sim\chi_0-(-1)^{i_x+j_y}\Delta_0 v_{ij}, \tag{4.4}$$

$$\tilde{\Delta}_{ij}\sim\Delta_0+(-1)^{i_x+j_y}\chi_0 v_{ij}, \tag{4.5}$$

which give $\overline{U}^d_{ij}=U^d_{ij}+\delta U_{ij}$ with

$$\delta U_{ij}=(-1)^{i_x+j_y}[\Delta_0\tau^3+(-1)^{i_y+j_y}\chi_0\tau^1]v_{ij}. \tag{4.6}$$

Then, we treat the term

$$\delta H^F=\frac{\tilde{J}}{2}\sum_{\langle i,j\rangle}\psi^\dagger_i\,\delta U_{ij}\psi_j \tag{4.7}$$

as perturbation with respect to H^F_0 where $\mathbf{a}_{0i}$ is given by Eq. (3.18). The free propagation is governed by U^d_{ij} and the corresponding propagator becomes

$$\mathcal{G}^F_0(\mathbf{k},i\omega)=\frac{U_\mathbf{k}}{i\omega-E_\mathbf{k}}+\frac{V_\mathbf{k}}{i\omega+E_\mathbf{k}}, \tag{4.8}$$

where the generalized coherence factors are introduced by $U_\mathbf{k}=\frac{1}{2}[1+(\gamma_\mathbf{k}\tau^3+\eta_\mathbf{k}\tau^1)/E_\mathbf{k}]$ and $V_\mathbf{k}=\frac{1}{2}[1-(\gamma_\mathbf{k}\tau^3+\eta_\mathbf{k}\tau^1)/E_\mathbf{k}]$. The one-particle spectrum is given by

$$E_\mathbf{k}=\sqrt{\gamma_k^2+\eta_k^2}; \tag{4.9}$$

with $\gamma_\mathbf{k}=-\tilde{J}\chi_0[\cos k_x+\cos k_y+\tilde{t}_2\cos k_x\cos k_y+\tilde{t}_3(\cos 2k_x+\cos 2k_y)]+a_0$ and $\eta_\mathbf{k}=+\tilde{J}\Delta_0(\cos k_x-\cos k_y)$. We have taken account of the second and third nearest-neighbor hopping of the fermions to reproduce the real band structure. In general, the *d*-wave nodes shift from $(\pm\pi/2,\pm\pi/2)$. In the case of $t_2=t_3=0$, the nodes are located at $(\pm\cos^{-1}[a_0/2\tilde{J}\chi_0],\pm\cos^{-1}[a_0/2\tilde{J}\chi_0])$. For $\tilde{t}_2\neq 0$ and $\tilde{t}_3\neq 0$, the nodes are located at $(\pm\cos^{-1}[f(\tilde{t}_2,\tilde{t}_3,a_0)],\pm\cos^{-1}[f(\tilde{t}_2,\tilde{t}_3,a_0)])$, where

$$f(\tilde{t}_2,\tilde{t}_3,a_0)=\frac{-1+\sqrt{1+(4\tilde{t}_3+\tilde{t}_2)(2\tilde{t}_3+a_0/\tilde{J}\chi_0)}}{4\tilde{t}_3+\tilde{t}_2}. \tag{4.10}$$

We see that as far as $\tilde{t}_3\neq 0$ the nodes shift from $(\pm\pi/2,\pm\pi/2)$ even if $a_0=0$. Furthermore, we note that location of the nodes is independent of the gap magnitude Δ_0.

Since the perturbation term causes period doubling, it is convenient to introduce the fermion operators on two sublattices,

$$\psi_i=\frac{1}{\sqrt{2}}\sum_{\mathbf{k}\in\mathrm{RZ}}e^{i\mathbf{k}\cdot\mathbf{r}_i}(\psi_\mathbf{k}\pm\psi_{\mathbf{k}+\mathbf{Q}}), \tag{4.11}$$

where $\mathbf{Q}=(\pi,\pi)$ and $\mathbf{k}\in\mathrm{RZ}$ means $\mathbf{k}$ runs over the reduced Brillouin zone $|k_z|+|k_y|\leqslant\pi$. We have dropped the spin indices. The + and − signs are for the cases where *i* belongs to the *A* $[\mathbf{r}_i=(i_x,i_y)=$(even,even) or (odd, odd)] and *B* $[(i_x,i_y)=$(even,odd) or (odd, even)] sublattice sites, respectively. Then, as derived in Appendix C, the perturbation term is written in momentum space as

$$\delta H^F=-\sum_{\mathbf{k}\in\mathrm{RZ}}\sum_{\mathbf{q},\sigma}[\psi^\dagger_{\mathbf{k}+\mathbf{q}/2+\mathbf{Q}\sigma}C_\mathbf{k}(\mathbf{q})\psi_{\mathbf{k}-(\mathbf{q}/2)\sigma}+\mathrm{H.c.}], \tag{4.12}$$

where $C_\mathbf{k}(\mathbf{q})=\Delta_0 C^+_\mathbf{k}(\mathbf{q})\tau^3+\chi_0 C^-_\mathbf{k}(\mathbf{q})\tau^1$ with

$$\mathcal{C}^\pm_\mathbf{k}(\mathbf{q})=\pi\tilde{J}\frac{1}{|\mathbf{q}|^2}\frac{\lambda_a|\mathbf{q}|}{1+\lambda_a|\mathbf{q}|}[q_y\sin k_x\pm q_x\sin k_y]. \tag{4.13}$$

The momentum transfer **q** should be small because we have retained only slowly varying **v** field. The perturbation processes cause unit-cell doubling and scatter the electron with **k** in the reduced zone to $\mathbf{k}+\mathbf{Q}$ in the second zone, and consequently the mirror image of the reduced zone is formed in the second zone, as indicated in Fig. 7(a).

Now, we consider the four distinct points on lattice indicated in Fig. 6: (a) the center of the plaquette (plaquette center), (b) the top of the sites (site top), and (c) the center of the bonds (bond center). The site-top and bond-center points correspond to the Cu and the O sites, respectively, on the CuO_2 plane. All the detail of derivation of the LDOS is left to Appendix C. In any case, the LDOS is written in a form

$$N(\mathbf{r},\omega)/x\alpha^2=\overline{N}_0(\omega)\pm\delta\overline{N}(\mathbf{r},\omega), \tag{4.14}$$

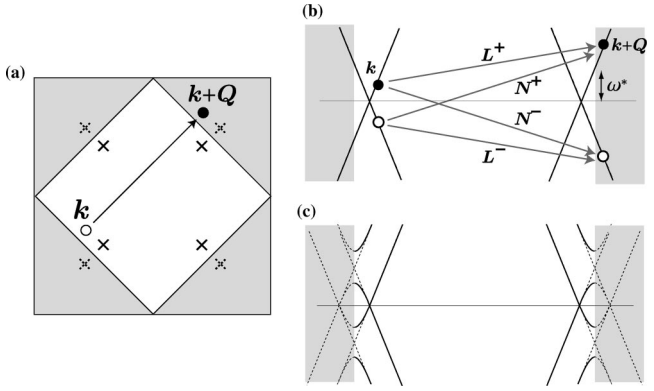

FIG. 7. (a) The perturbation processes given by Eq. (4.7) connect the electron with $\mathbf{k}$ in the reduced zone (inner square) to $\mathbf{k}+\mathbf{Q}$ in the second zone (shaded region), and consequently the mirror image of the reduced zone is formed in the second zone. The *d*-wave nodes inside the reduced zone and their mirror images are also indicated. (b) The scattering processes along the (0,0) $\rightarrow(\pi,\pi)$ direction whose matrix elements give the coherence factors $L_{\mathbf{k}}^{\pm}$ and $N_{\mathbf{k}}^{\pm}$. At the energy ω^*, the Dirac cones around the *d*-wave nodes touch the reduced zone boundary and resonance occurs. (c) The level crossing at the reduced zone boundary would be lifted and eventually the period doubling would cause gap opening if we would go beyond the perturbative scheme. Note that situations in (b) and (c) correspond to the case of a simple band structure without the next ($\tilde{t}_2$) and second nearest ($\tilde{t}_3$) fermion hopping.

where + and − signs alternate from plaquette to plaquette, site to site, or bond to bond for the cases (a), (b), and (c), respectively, and α represents magnitude of the envelope function from the nearest cite. The uniform counterparts are given in a form

$$\overline{N}_0(\omega)=-\frac{1}{\pi}\mathrm{Im}\sum_{\mathbf{k}} M_0(\mathbf{k})[\mathcal{G}^F(\mathbf{k},\mathbf{k},i\omega)]_{11}|_{i\omega\rightarrow\omega+i\delta}, \tag{4.15}$$

where we introduced the generalized propagator $\mathcal{G}^F(\mathbf{k},\mathbf{k}',i\omega)=\Sigma_{\mathbf{r}_i,\mathbf{r}_j}e^{i(\mathbf{k}\cdot\mathbf{r}_i-\mathbf{k}\cdot\mathbf{r}_j)}\mathcal{G}^F_{ij}(i\omega)$. The matrix elements $M_0(\mathbf{k})$ distinguishes different symmetries associated with each point and are given by

$$M_0^{\mathrm{plaquctte}}(\mathbf{k})=\cos^2\frac{k_x}{2}\cos^2\frac{k_y}{2}, \tag{4.16}$$

$$M_0^{\mathrm{site}}(\mathbf{k})=1, \tag{4.17}$$

$$M_0^{\mathrm{bond}}(\mathbf{k})=\cos^2\frac{k_x}{2}. \tag{4.18}$$

for the cases (a), (b), and (c), respectively. The perturbation processes do not affect the uniform counterpart within the Born approximation, and thus, in Eq. (4.15), we obtain

$$\begin{aligned}&\mathrm{Im}[\mathcal{G}^F(\mathbf{k},\mathbf{k},i\omega)]_{11}|_{i\omega\rightarrow\omega+i\delta}\\&=\mathrm{Im}[\mathcal{G}_0^F(\mathbf{k},i\omega)]_{11}|_{i\omega\rightarrow\omega+i\delta}\\&=\frac{\pi}{2}\left(1+\frac{\gamma_k}{E_{\mathbf{k}}}\right)\delta(\omega-E_{\mathbf{k}})+\frac{\pi}{2}\left(1-\frac{\gamma_k}{E_{\mathbf{k}}}\right)\delta(\omega+E_{\mathbf{k}}),\end{aligned} \tag{4.19}$$

which just reproduces the LDOS profile in the uniform *d*-wave SC state except overall reduction due to the matrix element $M_0(\mathbf{k})$.

The staggered counterpart is given in a form

$$\begin{aligned}\delta\overline{N}(\mathbf{r},\omega)=-\frac{1}{\pi}\mathrm{Im}\sum_{\mathbf{q}\sim\mathrm{small}}\sum_{\mathbf{k}\in\mathrm{RZ}}M(\mathbf{k},\mathbf{q};\mathbf{r})\Bigg[\mathcal{G}^F\Bigg(\mathbf{k}+\frac{\mathbf{q}}{2}\\+\mathbf{Q},\mathbf{k},-\frac{\mathbf{q}}{2},i\omega\Bigg)+\mathcal{G}^F\Bigg(\mathbf{k}-\frac{\mathbf{q}}{2},\mathbf{k}+\frac{\mathbf{q}}{2}\\+\mathbf{Q},i\omega\Bigg)\Bigg]_{11}\Bigg|_{i\omega\rightarrow\omega+i\delta},\end{aligned} \tag{4.20}$$

The matrix elements $M(\mathbf{k},\mathbf{q};\mathbf{r})$ associated with each point are given by

$$\begin{aligned}M^{\mathrm{plaquette}}(\mathbf{k},\mathbf{q};\mathbf{r})=\cos(\mathbf{q}\cdot\mathbf{r})\sin\frac{k_x+\frac{q_x}{2}}{2}\\\times\sin\frac{k_y+\frac{q_y}{2}}{2}\cos\frac{k_x-\frac{q_x}{2}}{2}\cos\frac{k_y-\frac{q_y}{2}}{2},\end{aligned} \tag{4.21}$$

$$M^{\mathrm{site}}(\mathbf{k},\mathbf{q};\mathbf{r})=\cos(\mathbf{q}\cdot\mathbf{r}), \tag{4.22}$$

$$M^{\mathrm{bond}}(\mathbf{k},\mathbf{q};\mathbf{r})=\sin(\mathbf{q}\cdot\mathbf{r})\sin\frac{k_x+q_x/2}{2}\cos\frac{k_x-q_x/2}{2}, \tag{4.23}$$

where $\mathbf{r}$ denotes the plaquette-center, site-top, and bond-center points, respectively. Now we need to compute $\mathcal{G}^F(\mathbf{k}+\mathbf{q}/2+\mathbf{Q},\mathbf{k}-q/2,i\omega)$ and $\mathcal{G}^F(\mathbf{k}-q/2,\mathbf{k}+\mathbf{q}/2+\mathbf{Q},i\omega)$. The detail of computation is presented in Appendix C. We obtain

$$\begin{aligned}&\Bigg[\mathcal{G}^F\Bigg(\mathbf{k}+\frac{\mathbf{q}}{2}+\mathbf{Q},\mathbf{k}-\frac{\mathbf{q}}{2},i\omega\Bigg)\\&\quad+\mathcal{G}^F\Bigg(\mathbf{k}-\frac{\mathbf{q}}{2},\mathbf{k}+\frac{\mathbf{q}}{2}+\mathbf{Q},i\omega\Bigg)\Bigg]_{11}\Bigg|_{i\omega\rightarrow\omega+i\delta}\\&=-\frac{\pi}{2}\delta(\omega,+E_{\mathbf{k}+\mathbf{q}/2+\mathbf{Q}},E_{\mathbf{k}-\mathbf{q}/2})[\Delta_0\mathcal{C}_{\mathbf{k}}^{+}(\mathbf{q})L_k^{\Delta+}\\&\quad+\chi_0\mathcal{C}_{\mathbf{k}}^{-}(\mathbf{q})L_{\mathbf{k}}^{\chi+}]+\frac{\pi}{2}\delta(\omega,-E_{\mathbf{k}+\mathbf{q}/2+\mathbf{Q}},-E_{\mathbf{k}-\mathbf{q}/2})\end{aligned}$$

$$
\begin{aligned}
&[\Delta_0 \mathcal{C}^+_{\mathbf{k}}(\mathbf{q}) L^{\Delta-}_{\mathbf{k}} + \chi_0 \mathcal{C}^-_{\mathbf{k}}(\mathbf{q}) L^{\chi-}_{k}] \\
&\quad - \frac{\pi}{2}\,\delta(\omega, +E_{\mathbf{k}+\mathbf{q}/2+\mathbf{Q}}, -E_{\mathbf{k}-\mathbf{q}/2}) \\
&\quad \times [\Delta_0 \mathcal{C}^+_{\mathbf{k}}(\mathbf{q}) N^{\Delta+}_{\mathbf{k}} + \chi_0 \mathcal{C}^-_{\mathbf{k}}(\mathbf{q}) N^{\chi+}_{\mathbf{k}}] \\
&\quad + \frac{\pi}{2}\,\delta(\omega, -E_{\mathbf{k}+\mathbf{q}/2+\mathbf{Q}}, +E_{\mathbf{k}-\mathbf{q}/2}) \\
&\quad \times [\Delta_0 \mathcal{C}^+_{\mathbf{k}}(\mathbf{q}) N^{\Delta-}_{\mathbf{k}} + \chi_0 \mathcal{C}^-_{\mathbf{k}}(\mathbf{q}) N^{\chi-}_{\mathbf{k}}], \qquad (4.24)
\end{aligned}
$$

where $\delta(\omega,x,y) \equiv [\delta(\omega-x)-\delta(\omega-y)]/(x-y)$. The coherence factors are given by

$$
\begin{aligned}
L^{\Delta\pm}_{\mathbf{k}} &= 1 + \gamma_+\gamma_- - \eta_+\eta_- \pm \gamma_+ \pm \gamma_-, \\
L^{\chi\pm}_{\mathbf{k}} &= \pm\eta_+ \pm \eta_- + \gamma_+\eta_- + \eta_+\eta_-, \\
N^{\Delta\pm}_{\mathbf{k}} &= 1 - \gamma_+\gamma_- + \eta_+\eta_- \pm \gamma_+ \mp \gamma_-, \\
N^{\chi\pm}_{\mathbf{k}} &= \pm\eta_+ \mp \eta_- - \gamma_+\eta_- - \eta_+\gamma_-, \qquad (4.25)
\end{aligned}
$$

where $\gamma_+ = \gamma_{\mathbf{k}+\mathbf{q}/2+\mathbf{Q}}/E_{\mathbf{k}+\mathbf{q}/2+\mathbf{Q}}$, $\gamma_- = \gamma_{\mathbf{k}-\mathbf{q}/2}/E_{\mathbf{k}-\mathbf{q}/2}$, $\eta_+ = \eta_{\mathbf{k}+\mathbf{q}/2+\mathbf{Q}}/E_{\mathbf{k}+\mathbf{q}/2+\mathbf{Q}}$, and $\eta_- = \eta_{\mathbf{k}-\mathbf{q}/2}/E_{\mathbf{k}-\mathbf{q}/2}$.

To proceed with further analytical computation, we note that the main contribution of **k** integral comes from regions near the nodes in the vicinity of $(\pm\pi/2,\pm\pi/2)$, while **q** is small. Thus, it is legitimate to ignore **q** with respect to **k** in $M_0(\mathbf{k})$, $M(\mathbf{k},\mathbf{q};\mathbf{r})$, and $\mathcal{G}^F(\mathbf{k}+\mathbf{q}/2+\mathbf{Q},\mathbf{k}-\mathbf{q}/2,i\omega)$, while we must retain **q** in $C^{\pm}_{\mathbf{k}}(\mathbf{q})$. This approximation amounts to ignoring the **r** dependence of the $\mathbf{v}(\mathbf{r})$ field over the lattice scales, and retaining only fermion fluctuations. On the other hand, retaining **q** dependence of $C^{\pm}_{\mathbf{k}}(\mathbf{q})$ amounts to taking account of the long-distance decay of the **v** field. Under this approximation. Eqs. (4.21), (4.22), and (4.23) are simply reduced to

$$
M^{\text{plaquette}}(\mathbf{k},\mathbf{q};\mathbf{r}) = \tfrac{1}{4}\cos(\mathbf{q}\cdot\mathbf{r})\sin k_x \sin k_y, \qquad (4.26)
$$

$$
M^{\text{site}}(\mathbf{k},\mathbf{q};\mathbf{r}) = \cos(\mathbf{q}\cdot\mathbf{r}), \qquad (4.27)
$$

$$
M^{\text{bond}}(\mathbf{k},\mathbf{q};\mathbf{r}) = \tfrac{1}{2}\sin(\mathbf{q}\cdot\mathbf{r})\sin k_x. \qquad (4.28)
$$

By noting the antisymmetry relation $\mathcal{C}^{\pm}_{\mathbf{k}}(\mathbf{q}) = -\mathcal{C}^{\pm}_{\mathbf{k}}(-\mathbf{q})$, we immediately see that $\delta\overline{N}(\mathbf{r},\omega)$ vanishes at the plaquette-center and site-top points while it remains finite at the bond-center points. Thus, we confirm that *the staggered counterpart of the LDOS appears only when measured on the bonds*. Even in the cases of the plaquette center and the site top, $\delta\overline{N}(\mathbf{r},\omega)$ becomes finite if we retain **q** with respect to **k**, i.e., taking account of the negligibly small dependence of the **v** field on the spatial position **r** over the lattice scales. However, this effect is still invisibly small as compared with the case of the bond center. This result is fully consistent with an intuitive discussion given in Sec. IV A.

From now on, we concentrate on the bond-center points: the midpoint of the bond connecting **i** and $\mathbf{i}+\hat{\mathbf{e}}_\mu$ where $\mu = x$ or y. Taking account of the envelope function, the magnitude of the LDOS may be reduced by a factor $e^{-2} \sim 0.1$ as compared with the uniform counterpart of the LDOS at the site top. Using Eqs. (4.24) and (4.28), the **q** integration in Eq. (4.20) can be performed to yield

$$
\begin{aligned}
\delta\overline{N}(\mathbf{r},\omega) = \frac{(-1)^{i_x+i_y}}{4} v_\mu(\mathbf{r}) \sum_{\mathbf{k}\in \mathrm{RZ}} \sin^2 k_\mu \\
\times [L^+_{\mathbf{k}}\,\delta(\omega; E_{\mathbf{k}}, E_{\mathbf{k}+\mathbf{Q}}) + L^-_{\mathbf{k}}\,\delta(\omega; -E_{\mathbf{k}}, -E_{\mathbf{k}+\mathbf{Q}}) \\
+ N^+_{\mathbf{k}}\,\delta(\omega; E_{\mathbf{k}}, -E_{\mathbf{k}+\mathbf{Q}}) + N^-_{\mathbf{k}}\,\delta(\omega; -E_{\mathbf{k}}, E_{\mathbf{k}+\mathbf{Q}})], \qquad (4.29)
\end{aligned}
$$

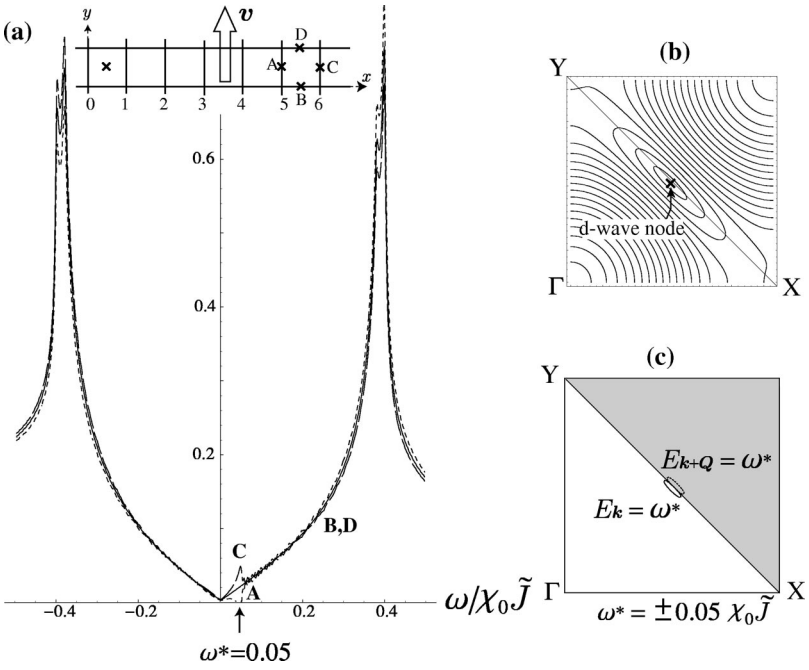

FIG. 8. (a) LDOS profile in the case of $t_2 = t_3 = 0$, obtained by the perturbative analysis at the points *A*, *B*, *C*, and *D* indicated in the inset. The LDOS at *B* and *D* are just $\overline{N}_0(\omega)$. The peaks at $\tilde{\omega} = \omega/\chi_0\tilde{J} = \pm 0.38$ are associated with the *d*-wave superconducting gap. The additional peaks at $\tilde{\omega} = \pm 0.41$ are associated with the van Hove singularity located at $(0, \pm\pi)$ and $(\pm\pi, 0)$. The staggered structure around $\tilde{\omega} = 0.05$ comes from resonant scattering between the fermions with **k** and $\mathbf{k}+\mathbf{Q}$, caused by the period doubling. (b) The one-particle energy contour around the *d*-wave node. (c) The energy contours $E_{\mathbf{k}} = \omega$ and $E_{\mathbf{k}+\mathbf{Q}} = \omega$ touch at $\tilde{\omega} = \pm 0.05$.

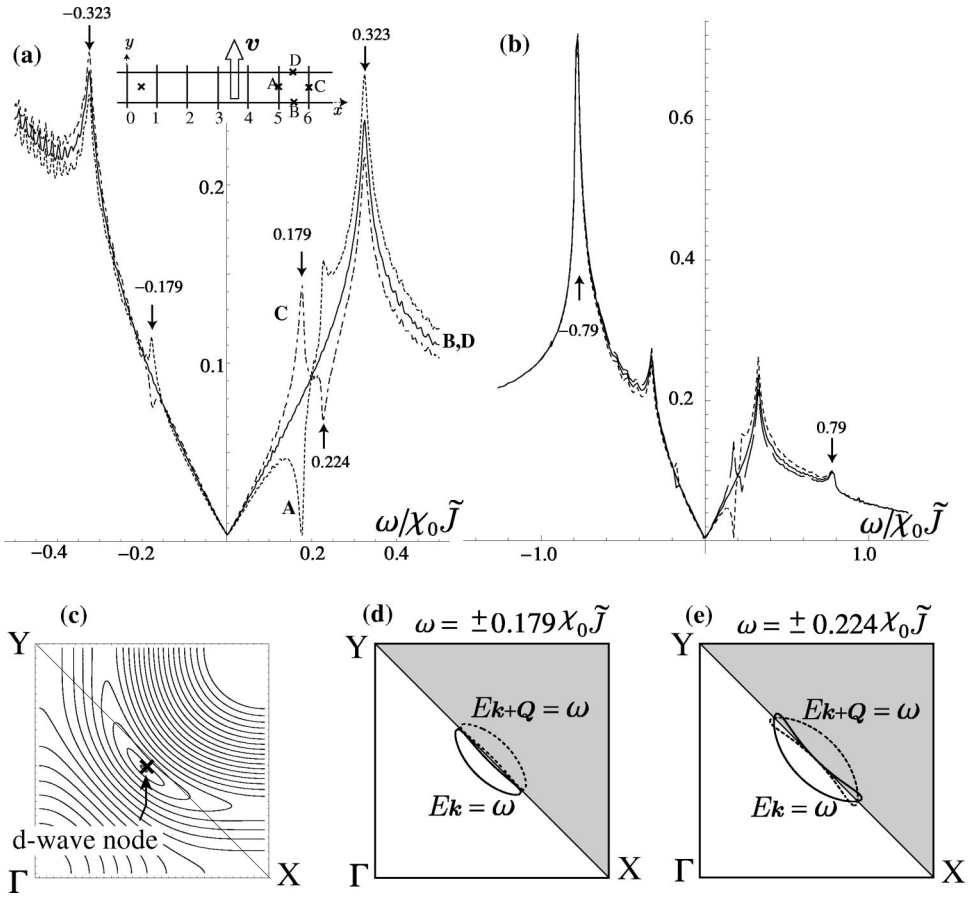

FIG. 9. (a) LDOS profile in the case of the real band structure of BSCCO, obtained by the perturbative analysis at the points *A*, *B*, *C*, and *D* indicated in the inset. The LDOS at *B* and *D* are just $\tilde{N}_0(\omega)$. The staggered structure around $\tilde{\omega} = \pm 0.179$ and $\tilde{\omega} = 0.224$ comes from resonant scattering between the fermions with $\mathbf{k}$ and $\mathbf{k}+\mathbf{Q}$ caused by the period doubling. The small wiggles outside the V-shaped profile come from numerical fluctuations. (b) The profile over a wider energy window than that of (a). The peaks at $\tilde{\omega} = \pm 0.79$ are ascribed to the van-Hove singularity at $(0, \pm\pi)$ and $(\pm\pi, 0)$ points. (c) The one-particle energy contour around the *d*-wave node. The energy contours $E_{\mathbf{k}} = \omega$ and $E_{\mathbf{k}+\mathbf{Q}} = \omega$ touch at $\tilde{\omega} = \pm 0.179$ and ± 0.224 as indicated in (d) and (e), respectively.

where the coherence factors $L^{\pm}_{\mathbf{k}} = \Delta_0 L^{\Delta\pm}_{\mathbf{k}} + \chi_0 L^{\chi\pm}_{\mathbf{k}}$ and $N^{\pm}_{\mathbf{k}} = \Delta_0 N^{\Delta\pm}_{\mathbf{k}} + \chi_0 N^{\chi\pm}_{\mathbf{k}}$ represent the matrix element associated with the scattering processes indicated in Fig. 7(b). As has already been mentioned, the best paths to detect the staggered modulation of the LDOS are the lines $i_x = \frac{1}{2}$ or $i_y = \frac{1}{2}$ provided that the vortex center sits at $(\frac{1}{2}, \frac{1}{2})$, because in this case we can go through the bonds whose directions $\hat{\mathbf{e}}_\mu$ are parallel to the circulating $\mathbf{v}(\mathbf{r})$ field (see Fig. 5).

1. The case of $t_2 = t_3 = 0$

First, we consider a toy band structure with $t_2 = t_3 = 0$ in Eq. (4.9), because this simple case provides us with a clear view on the period-doubling effects. In Fig. 8(a), we show the profile of $N(\mathbf{r}, \omega)/x\alpha^2$ at the four bond-center points, $A(i_x, \frac{1}{2})$, $B(i_x + \frac{1}{2}, 0)$, $C(i_x + 1, \frac{1}{2})$, and $D(i_x + \frac{1}{2}, 1)$ with $i_x = 5$ [see the inset of Fig. 8(a)]. From now on, we fix the parameters $a_0 = 0.05\chi_0\tilde{J}$, $\Delta_0/\chi_0 = 0.2$, and assume the gauge-field-penetration depth to be $\lambda_a = 10$. This choice of a_0 and Δ_0 is reasonable in the underdoped regime.[12] Note that at *B* and *D*, $\Delta\overline{N}(\mathbf{r}, \omega)$ almost vanishes and the LDOS is just given by $\overline{N}_0(\omega)$, because $\mathbf{v}(\mathbf{r})$ becomes almost perpendicular to these bond directions. The modulation pattern at the other points can be read off from Fig. 5.

We see that inside the overall V-shaped profile with the sharp peaks at $\tilde{\omega} \equiv \omega/\chi_0\tilde{J} = \pm 0.38$ associated with the *d*-wave superconducting gap, there appear additional peak and dip structures at site *C* and *A*, respectively, around $\tilde{\omega} = +0.05$. From now on, we refer to this structure as the ''staggered peak-dip (SPD)'' structure, since the peak and dip alternate from bond to bond in a staggered manner. The additional peaks at $\tilde{\omega} = \pm 0.41$ come from the van Hove singularity located at $(0, \pm\pi)$ and $(\pm\pi, 0)$ points. The low-energy dispersion gives elliptic contours around the *d*-wave node as indicated in Fig. 8(b), which touch the reduced zone boundary at $(\pi/2, \pi/2)$ as the energy increases. The specific structure around $\tilde{\omega} = 0.05$ comes from resonant scattering between the fermions with $\mathbf{k}$ and $\mathbf{k}+\mathbf{Q}$. As ω increases from zero, the energy contours $E_{\mathbf{k}} = \omega$ and $E_{\mathbf{k}+\mathbf{Q}} = \omega$ touch at $(\pi/2, \pi/2)$ on the reduced zone boundary at $\tilde{\omega} = \pm 0.05$ as indicated in Fig. 8(c) [see also Fig. 7(b)] and resonance occurs. We note that the modulated structure inside the V-shaped profile is predominant on the particle side $(\omega > 0)$. This asymmetry is due to the matrix-element effect: $L^{-}_{\mathbf{k}}$ vanishes at $(\pi/2, \pi/2)$.

In any case of this toy band structure, it may be totally hopeless to experimentally detect such tiny structures as indicated in Fig. 8(a). We see in the following that the realistic band structure of BSCCO drastically changes this situation.

2. The case of real band structure

Next, we take account of $\tilde{t}_2 = -0.550$ and $\tilde{t}_3 = 0.087$ to reproduce the real band structure of BSCCO measured by angle-resolved photoemission spectroscopy.[36] In Fig. 9(a), we show the profile of $N(\mathbf{r}, \omega)/x\alpha^2$ at the same points as in Fig. 8(a). In this case, inside the overall V-shaped profile with the sharp peaks at $\tilde{\omega} \equiv \omega/\chi_0\tilde{J} = \pm 0.323$ associated with

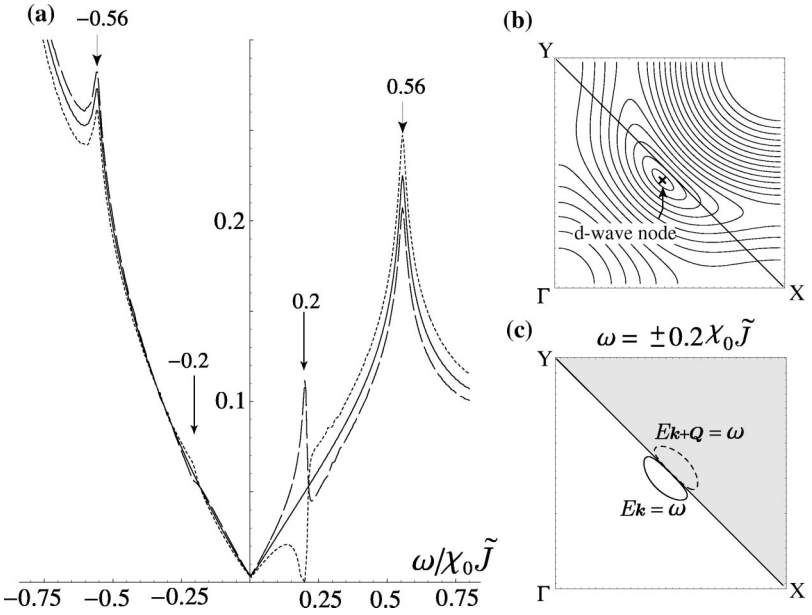

FIG. 10. (a) LDOS profile for $a_0 = 0.03\chi_0\tilde{J}$ and $\Delta_0/\chi_0 = 0.35$, corresponding to lower doping as compared with the case of $a_0 = 0.05\chi_0\tilde{J}$. (b) The one-particle energy contour around the *d*-wave node. The energy contours $E_{\mathbf{k}} = \omega$ and $E_{\mathbf{k}+\mathbf{Q}} = \omega$ touch at $\tilde{\omega} = \pm 0.2$ as indicated in (c).

the *d*-wave superconducting gap, there appears a prominent SPD structure around $\tilde{\omega} = \pm 0.179$ and $\tilde{\omega} = 0.224$. In Fig. 9(b), we show the same profile as in Fig. 9(a) over a wider energy window. The peaks at $\tilde{\omega} = \pm 0.79$ are ascribed to the van Hove singularity at $(0, \pm\pi)$ and $(\pm\pi, 0)$ points.[37]

The SPD structure inside the V-shaped profile again comes from resonant scattering between the fermions with $\mathbf{k}$ and $\mathbf{k}+\mathbf{Q}$. As seen in Fig. 9(c), the low-energy elliptic contours in the case without t_2 and t_3 [Fig. 8(b)] bend around the *d*-wave nodes (bending of the Dirac cone). Consequently, as ω increases from zero, the energy contours $E_{\mathbf{k}} = \omega$ and $E_{\mathbf{k}+\mathbf{Q}} = \omega$ first touch on the reduced zone boundary at $\tilde{\omega} = \pm 0.179$ as indicated in Fig. 9(d), and resonance occurs. Then, at $\tilde{\omega} = \pm 0.22$ they touch again at $(\pi/2, \pi/2)$ as indicated in Fig. 9(c) and the second resonance occurs. The reason why the second resonance comes up only in the electron $(\omega > 0)$ side is again ascribed to the matrix-element effect as in the case of $t_2 = t_3 = 0$. We can say that *due to the real band structure* (*bending of the Dirac cones around the d-wave nodes*) *the staggered structure in the LDOS* profile becomes far more prominent as compared with the case of $t_2 = t_3 = 0$.

We see that the SPD structure due to the period doubling occurs only inside the V-shaped profile [see Fig. 9(b)]. In fact, the energy scale at which the SPD structure appears depends on the band-structure parameters ($a_0 \propto x$, Δ_0/χ_0, t_2, and t_3). For a reasonable choice of parameters in the underdoped regime, however, the resonance always occurs at the energy scales below that of the superconducting gap, i.e., the SPD structure always appears inside the V-shaped profile.

To see a qualitative feature of the doping dependence, in Fig. 10(a) we show the LDOS profile for $a_0 = 0.03\chi_0\tilde{J}$ and $\Delta_0/\chi_0 = 0.35$, corresponding to the case of a lower doping as compared with the case of $a_0 = 0.05\chi_0\tilde{J}$ and $\Delta_0/\chi_0 = 0.2$. We see that the SPD structure remains robust, although the resonance occurs only once at $\tilde{\omega} = 0.2$. Smearing out of the second resonance is due to change of the geometry of the Dirac cone around the *d*-wave nodes. The shape of the low-energy contours changes upon changing Δ as clearly seen by comparing Fig. 10(b) with Fig. 9(c). The contours $E_{\mathbf{k}} = \omega$ and $E_{\mathbf{k}+\mathbf{Q}} = \omega$ touch on the reduced zone boundary only at $\tilde{\omega} = \pm 0.2$ [Fig. 10(c)]. As already mentioned, however, location of the *d*-wave nodes is independent of Δ_0 and always shifts from $(\pm\pi/2, \pm\pi/2)$ for finite $\tilde{t}_3$, i.e., the resonance at $(\pm\pi/2, \pm\pi/2)$ occurs at the energy

$$\tilde{\omega}^* = \pm(2\tilde{t}_3 + a_0/\chi_0\tilde{J}). \tag{4.30}$$

In this respect, *the next-nearest-neighbor hopping $\tilde{t}_3$ plays a crucial role in pushing the energy scales of the SPD structure toward visibly finite energy scales*.

In the perturbative picture presented here, the period-doubled perturbation processes form the ''mirror image'' of the energy bands with respect to the reduced zone boundary [Fig. 7(a)]. The energy level $E_{\mathbf{k}}$ and its mirror image $E_{\mathbf{k}+\mathbf{Q}}$ cross on the zone boundary $|k_x| + |k_y| = \pi$, which causes the resonant scattering at the corresponding energy ω^* [Fig. 7(b)]. It is naturally expected that if we go beyond the perturbative scheme the level crossing would be lifted and eventually the period doubling may cause a gap opening in the fermion excitation spectrum as indicated in Fig. 7(c). This point is confirmed through the exact diagonalization under uniform-**v** approximation as shown below.

C. Exact diagonalization after the uniform-*v* approximation

Next we consider the case of uniform $\mathbf{v}$ field $\mathbf{v}_0 = (v_{0x}, v_{0y})$, which may locally capture the effects of the circulating $\mathbf{v}(\mathbf{r})$. From Eqs. (3.5), (3.15), and (3.16), we see that uniform $\mathbf{v}_0$ yields

$$\overline{\chi}_{ij} = \tilde{\chi}_{ij} = A\cos[\Phi_0 + (-1)^{i_x+j_y}(\mathbf{r}_i - \mathbf{r}_j)\cdot\mathbf{v}_0], \tag{4.31}$$

$$\overline{\Delta}_{ij} = \tilde{\Delta}_{ij} = A\sin[\Phi_0 + (-1)^{i_x+j_y}(\mathbf{r}_i - \mathbf{r}_j)\cdot\mathbf{v}_0]. \tag{4.32}$$

An advantage of the uniform-**v** approximation is that we can exactly diagonalize the corresponding fermion Hamiltonian, which can be written as

$$H_0^F=\frac{1}{2}\sum_{\mathbf{k}\in \mathrm{RZ}} \Psi_{\mathbf{k}\sigma}^{\dagger} T_{\mathbf{k}} \Psi_{\mathbf{k}\sigma}, \tag{4.33}$$

where $(\Psi_{\mathbf{k}\sigma})^T=([\psi_{\mathbf{k}\sigma}]^T,[\psi_{\mathbf{k}+\mathbf{Q}\sigma}]^T)$. The 4×4 matrix $\mathbf{T}_{\mathbf{k}}$ is given by

$$\mathbf{T}_{\mathbf{k}}=\begin{pmatrix} V_{\mathbf{k}}+a_{\mathbf{k}}\tau^3 & iW_{\mathbf{k}} \\ iW_{\mathbf{k}+\mathbf{Q}} & V_{\mathbf{k}+\mathbf{Q}}+a_{\mathbf{k}+\mathbf{Q}}\tau^3 \end{pmatrix}, \tag{4.34}$$

where $V_{\mathbf{k}}=-\chi_0\tilde{J}\tilde{\gamma}_{\mathbf{k}}\tau^3+\Delta_0\tilde{J}\tilde{\mu}_{\mathbf{k}}\tau^1$ and $W_{\mathbf{k}}=\Delta_0\tilde{J}\tilde{\lambda}_{\mathbf{k}}\tau^3+\chi_0\tilde{J}\tilde{\mu}_{\mathbf{k}}\tau^1$, with $\tilde{\gamma}_{\mathbf{k}}=\cos v_{0x}\cos k_x+\cos v_{0y}\cos k_y$, $\tilde{\eta}_{\mathbf{k}}=\cos v_{0x}\cos k_x-\cos v_{0y}\cos k_y$, $\tilde{\lambda}_{\mathbf{k}}=\sin v_{0x}\sin k_x+\sin v_{0y}\sin k_y$, $\tilde{\mu}_{\mathbf{k}}=\sin v_{0x}\sin k_x-\sin v_{0y}\sin k_y$. Noting the fact that the field **v** does not modulate the hopping amplitude between the same sublattice sites, we take account of the hopping parameters t_2 and t_3 by introducing

$$a_{\mathbf{k}}=a_0-\tilde{t}_2\cos k_x\cos k_y-\tilde{t}_3(\cos 2k_x+\cos 2k_y). \tag{4.35}$$

The one-particle propagator in a 4×4 matrix form is given by

$$\mathbf{G}^F(\mathbf{k},i\omega)=[i\omega\mathbf{1}-\mathbf{T}_{\mathbf{k}}]^{-1}, \tag{4.36}$$

where **1** denotes a 4×4 unit matrix. As was inferred from the perturbative analysis, the unit-cell doubling brings about the one-particle spectrum split into two branches in the reduced zone, $\pm E_{\mathbf{k}}^{+}$ and $\pm E_{\mathbf{k}}^{-}$, where

$$E_{\mathbf{k}}^{\pm}=[a_{\mathbf{k}}^2+\gamma_{\mathbf{k}}^2+\eta_{\mathbf{k}}^2+\lambda_{\mathbf{k}}^2+\mu_{\mathbf{k}}^2 \pm 2\{a_{\mathbf{k}}^2(\gamma_{\mathbf{k}}^2+\lambda_{\mathbf{k}}^2)+(\eta_{\mathbf{k}}\lambda_{\mathbf{k}}+\gamma_{\mathbf{k}}\mu_{\mathbf{k}})^2\}^{1/2}]^{1/2}, \tag{4.37}$$

with $\mathbf{k}\in$ RZ. To compute the LDOS, we need 11, 33, 13, and 31 components of $\mathbf{G}^F(\mathbf{k},i\omega)$, which are explicitly given in Appendix D.

As in the perturbative analysis, we consider the LDOS at four distinct points on the lattice: (a) the plaquette-center, (b) the site-top, and (c) the bond-center points. Repeating an analysis similar to that in Appendix C, we obtain the LDOS in a form

$$N(\omega)/x\alpha^2=\tilde{N}_0(\omega)\pm\delta\tilde{N}(\omega), \tag{4.38}$$

where + and − signs are alternated plaquette to plaquette, site to site, or bond to bond for the cases (a), (b), and (c), respectively. The uniform counterpart gives exactly the same form as in the case of the perturbative analysis,

$$\tilde{N}_0(\omega)=-\frac{1}{\pi}\mathrm{Im}\sum_k M_0(\mathbf{k})[\mathbf{G}^F(\mathbf{k},i\omega)]_{11}|_{i\omega\to\omega+i\delta}, \tag{4.39}$$

where $M_0(\mathbf{k})$ are given by Eqs. (4.16)–(4.18). We here used the relation $[\mathbf{G}^F(\mathbf{k},i\omega)]_{33}=[\mathbf{G}^F(\mathbf{k}+\mathbf{Q},i\omega)]_{11}$, which is explicitly shown in Appendix D.

The staggered counterparts at the plaquette-center and the site-top points are given in a form

$$\delta\tilde{N}(\omega)=-\frac{1}{\pi}\mathrm{Im}\sum_{\mathbf{k}\in \mathrm{RZ}} M(\mathbf{k})\times\{[\mathbf{G}^F(\mathbf{k},i\omega)]_{13}+[\mathbf{G}(\mathbf{k},i\omega)]_{31}\}|_{i\omega\to\omega+i\delta}, \tag{4.40}$$

where the matrix elements $M(\mathbf{k})$ are given by

$$M^{\mathrm{plaquette}}(\mathbf{k})=\sin k_x\sin k_y, \tag{4.41}$$

$$M^{\mathrm{site}}(\mathbf{k})=1. \tag{4.42}$$

As shown in Appendix D, we have the following relation: $[\mathbf{G}^F(\mathbf{k},i\omega)]_{13}=-[\mathbf{G}^F(\mathbf{k},i\omega)]_{31}=[\mathbf{G}^F(\mathbf{k},i\omega)]_{31}^{*}$. Therefore, $\delta\tilde{N}(\omega)$ exactly vanishes at the plaquette-center and site-top points.

On the other hand, at the bond-center points we obtain

$$\delta\tilde{N}(\omega)=-\frac{1}{\pi}\mathrm{Im}\sum_{\mathbf{k}\in \mathrm{RZ}} \sin k_\mu\{i[\mathbf{G}^F(\mathbf{k},i\omega)]_{13}-i[\mathbf{G}(\mathbf{k},i\omega)]_{31}\}|_{i\omega\to\omega+i\delta}, \tag{4.43}$$

which remains finite, where we considered the bond in the $\mathbf{e}_\mu$ direction. Thus, just as in the perturbative analysis, the LDOS exhibits staggered pattern only when measured on the bonds. Using an explicit form of $\mathbf{G}^F$ given in Appendix D, we obtain

$$\tilde{N}_0(\omega)=\sum_{\mathbf{k}} \cos^2\frac{k_z}{2}U_{\mathbf{k}}(\omega)[\delta(\omega-E_{\mathbf{k}}^{-})+\delta(\omega+E_{\mathbf{k}}^{-})-\delta(\omega-E_{\mathbf{k}}^{+})-\delta(\omega+E_{\mathbf{k}}^{+})], \tag{4.44}$$

$$\delta\tilde{N}(\omega)=\sum_{\mathbf{k}\in \mathrm{RZ}} \lambda_{\mathbf{k}}\tilde{U}_{\mathbf{k}}(\omega)\sin k_\mu[\delta(\omega-E_{\mathbf{k}}^{-})+\delta(\omega+E_{\mathbf{k}}^{-})-\delta(\omega-E_{\mathbf{k}}^{+})-\delta(\omega+E_{\mathbf{k}}^{+})], \tag{4.45}$$

where $U_{\mathbf{k}}(\omega)=[\omega^2+\omega A_{\mathbf{k}}-B_{\mathbf{k}}-C_{\mathbf{k}}/\omega]/2P_{\mathbf{k}}$ and $\tilde{U}_{\mathbf{k}}(\omega)=-[\omega+2a_{\mathbf{k}}+\tilde{C}_{\mathbf{k}}/\omega]/2P_{\mathbf{k}}$, with $P_{\mathbf{k}}, A_{\mathbf{k}},\ldots$ being given in Appendix D.

1. The case of $t_2=t_3=0$

First, we consider again a toy band structure with $t_2=t_3=0$ in Eq. (4.9). In Fig. 11(a), we show the profile of $\tilde{N}_0(\omega)$ and $\tilde{N}_0(\omega)\pm\delta\tilde{N}(\omega)$ for $\mathbf{v}_0=(0,0.1)$, of which direction and strength locally simulate $\mathbf{v}(\mathbf{r})$ around the points *B*, *D* and *A*, *C* in the inset of Fig. 8(a), respectively. We used the same parameter set as in the case of Fig. 8(a). In Fig. 11(b) is indicated the energy contour of the lower band $E_{\mathbf{k}}^{-}$ with the corresponding band structure of $E_{\mathbf{k}}^{\pm}$ being shown in Fig. 11(c). The uniform $\mathbf{v}_0$ field breaks the original four fold symmetry and the *d*-wave nodes are located slightly off the Γ-*M* line. The van Hove singularity on the *Y*-Γ line is caused solely by the superconducting gap and gives peaks at $\tilde{\omega}=\pm0.38$.

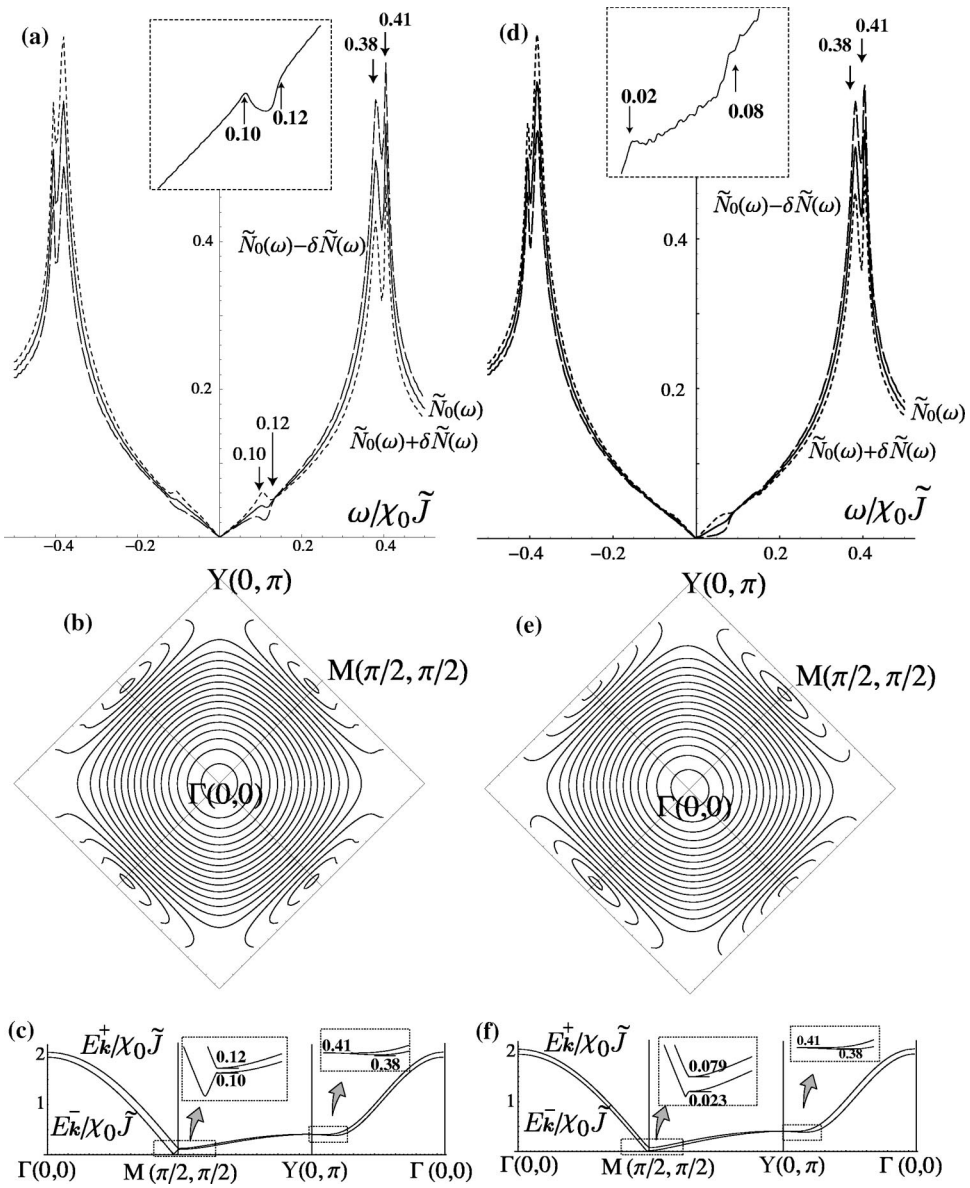

FIG. 11. (a) Profile of $\tilde{N}_0(\omega)$ and $\tilde{N}_0(\omega)\pm\delta\tilde{N}(\omega)$ for the uniform field $\mathbf{v}_0=(0,0.1)$ in the case of $t_2=t_3=0$. In the inset is shown fine structure of $\tilde{N}_0(\omega)$ around $\tilde{\omega}\sim 0.1$, detected with higher numerical resolution. (b) The energy contour of the lower band $E^-_{\mathbf{k}}$ and (c) the dispersion of $E^{\pm}_{\mathbf{k}}$ with $v_0=(0,0.1)$ along the path $\Gamma(0,0)\rightarrow M(\pi/2,\pi/2)\rightarrow Y(0,\pi)\rightarrow\Gamma$. Fine band splitting on the reduced zone boundary are magnified in the inset. (d) Profile of $\tilde{N}_0(\omega)$ and $\tilde{N}_0(\omega)\pm\delta\tilde{N}(\omega)$ for the uniform field $\mathbf{v}_0=(-0.1/\sqrt{2},0.1/\sqrt{2})$. In the inset is shown fine structure of $\tilde{N}_0(\omega)$ around $\tilde{\omega}\sim 0.05$, detected with higher numerical resolution. (e) The energy contour of the lower band $E^-_{\mathbf{k}}$ and (f) the dispersion of $E^{\pm}_{\mathbf{k}}$ with $\mathbf{v}_0=(-0.1/\sqrt{2},0.1/\sqrt{2})$. Fine band splittings on the reduced zone boundary are magnified in the inset.

As expected from the perturbative analysis, the unit-cell doubling causes the gap opening on the reduced zone boundary between $\tilde{\omega}=0.10$ and $\tilde{\omega}=0.12$. The van Hove singularities associated with this gap structure gives rise to the specific structure in the LDOS profile. The corresponding fine structure in $\tilde{N}_0(\omega)$ could be detected with much higher numerical resolution [720×720 meshes of the Brillouin zone], as shown in the inset of Fig. 11(a). The van Hove singularity at the $Y(0,\pi)$ point is intrinsic to the normal-state dispersion γ_k and gives peaks at $\tilde{\omega}=\pm 0.41$, just as in the case of Fig. 8(a).

We see that the staggered modulation profile shown in Fig. 11(a), $\tilde{N}_0(\omega)\pm\delta\tilde{N}(\omega)$, is in remarkable agreement with Fig. 8(a) obtained by the perturbative analysis. However, a striking difference is that the dip structure around $\tilde{\omega}=0.105$ is now intrinsic to the modified band structure with van Hove singularities associated with the gap opening on the reduced zone boundary and appears even in the uniform counterpart $\tilde{N}_0(\omega)$.

In Fig. 11(d), we show the LDOS profile for $\mathbf{v}_0=(-0.1/\sqrt{2},0.1/\sqrt{2})$, where the strength of $\mathbf{v}_0$ is the same as in the case of Fig. 8(a), but its direction locally simulates $\mathbf{v}(\mathbf{r})$ in the 45° direction in Fig. 5. In Fig. 11(c) is indicated the energy contour of the lower band $E^-_{\mathbf{k}}$ with the corresponding band structure of $E^{\pm}_{\mathbf{k}}$ being shown in Fig. 11(f). The uniform $\mathbf{v}_0=(-0.1/\sqrt{2},0.1/\sqrt{2})$ field breaks the original fourfold symmetry in a way different from the case of $\mathbf{v}_0=(0,0.1)$. Consequently, the energy scales of the van Hove singularities responsible for the dip structure move downward. The qualitative feature of the profile, however, does not change much for small magnitude of $\mathbf{v}_0$ considered here.

2. The case of real band structure

Next, we turn to the real band structure of BSCCO. In Fig. 12(a), we show the profile of $\tilde{N}_0(\omega)$ and $\tilde{N}_0(\omega)\pm\delta\tilde{N}(\omega)$ for $\mathbf{v}_0=(0,0.1)$, of which direction and strength locally simulate $\mathbf{v}(\mathbf{r})$ around the points *B*, *D* and *A*, *C* in the

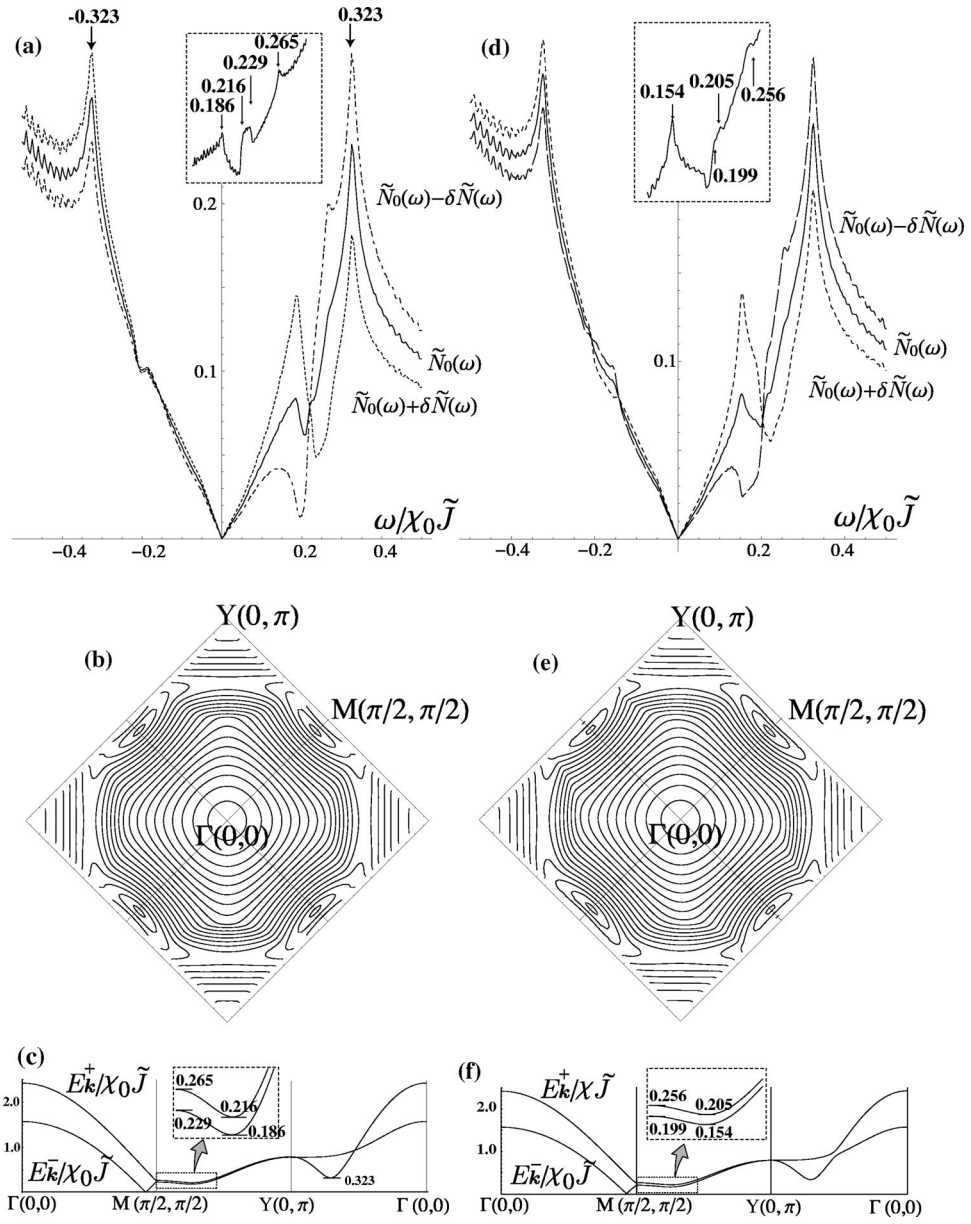

FIG. 12. (a) Profile of $\tilde{N}_0(\omega)$ and $\tilde{N}_0(\omega)\pm\delta\tilde{N}(\omega)$ for the uniform field $\mathbf{v}_0=(0,0.1)$ in the case of the real band structure of BSCCO. In the inset is shown fine structure of $\tilde{N}_0(\omega)$ around $\tilde{\omega}\sim 0.2$, detected with higher numerical resolution. (b) The energy contour of the lower band $E^-_{\mathbf{k}}$ and (c) the dispersion of $E^{\pm}_{\mathbf{k}}$ with $\mathbf{v}_0=(0,0.1)$ along the path $\Gamma(0,0)\rightarrow M(\pi/2,\pi/2)\rightarrow Y(0,\pi)\rightarrow\Gamma$. Fine band splitting on the reduced zone boundary are magnified in the inset. (d) Profile of $\tilde{N}_0(\omega)$ and $\tilde{N}_0(\omega)\pm\delta\tilde{N}(\omega)$ for the uniform field $\mathbf{v}_0=(-0.1/\sqrt{2},0.1/\sqrt{2})$. In the inset is shown fine structure of $\tilde{N}_0(\omega)$ around $\tilde{\omega}\sim 0.2$ detected with higher numerical resolution. (e) The energy contour of the lower band $E^-_{\mathbf{k}}$ and (f) the dispersion of $E^{\pm}_{\mathbf{k}}$ with $\mathbf{v}_0=(-0.1/\sqrt{2},0.1/\sqrt{2})$.

inset of Fig. 9(a), respectively. We used the same parameter set as in the case of Fig. 9(a). In Fig. 12(b) is indicated the energy contour of the lower band $E^-_{\mathbf{k}}$ with the corresponding band structure of $E^{\pm}_{\mathbf{k}}$ being shown in Fig. 12(c). The van Hove singularity on the Y-Γ line is caused solely by the superconducting gap and gives peaks at $\tilde{\omega}=\pm 0.323$. The uniform $\mathbf{v}_0$ field breaks the original fourfold symmetry and the d-wave nodes are located slightly off the Γ-M line. The unit-cell doubling causes the gap opening on the reduced zone boundary between $\tilde{\omega}=0.229$ and $\tilde{\omega}=0.265$, corresponding to the second resonance in the perturbative analysis [the second touch of the energy contour indicated in Fig. 9(d)]. In this case, due to the presence of t_2 and t_3, additional van Hove singularity occurs at $\tilde{\omega}=0.186$ and $\tilde{\omega}=0.216$, corresponding to the first resonance in the perturbative analysis [the first touch of the energy contour indicated in Fig. 9(c)]. The corresponding fine structure in $\tilde{N}_0(\omega)$ could be detected with much higher numerical resolution [720×720 meshes of the Brillouin zone], as shown in the inset of Fig. 2(A). As perturbative analysis, the van Hove singularity at the $Y(0,\pi)$ point is pushed upward as compared with the case of $t_2=t_3=0$ and lies at the energy $\tilde{\omega}=\pm 0.79$ outside the energy window of Fig. 12(a) just as in Fig. 9(b).

We see again that the profile in Fig. 12(a), in particular, the SPD structure inside the V-shaped profile, is in remarkable agreement with Fig. 9(a) obtained by the perturbative analysis. However, as in the case of $t_2=t_3=0$ a striking difference is that the SPD structure is now intrinsic to the modified band structure with van Hove singularities associated with the gap opening on the reduced zone boundary and appears even in the uniform counterpart $\tilde{N}_0(\omega)$. This suggests that in reality the SPD structure may be detected not only on the bonds but also at sites.

In Fig. 12(d), we show the LDOS profile for $\mathbf{v}_0=(-0.1/\sqrt{2},0.1/\sqrt{2})$, where the strength of $\mathbf{v}_0$ is the same as

in the case of Fig. 9(a), but its direction locally simulates $\mathbf{v}(\mathbf{r})$ in the 45° direction in Fig. 5. In Fig. 12(e) is indicated the energy contour of the lower band $E_{\mathbf{k}}^{-}$ with the corresponding band structure of $E_{\mathbf{k}}^{\pm}$ being shown in Fig. 12(f). The qualitative features of the LDOS profile given in Figs. 12(a) and 12(d) are quite similar. Thus, we may say that the SPD structure is robust and detectable in all the directions around the vortex center.

We note that in both perturbative and exact analysis, the SPD structure in the LDOS is predominant on the particle side ($\omega>0$). We can understand this asymmetry by first turning off the superconductivity and consider the effect of unit-cell doubling. Since we are doping with holes, the gaps being opened by unit-cell doubling are on the empty side on the Fermi surface. The matrix-element effect preserves this particle-hole asymmetry even after we turn on the superconductivity.

V. SUMMARY AND CONCLUDING REMARKS

In this paper, we have concentrated on how to detect a signature of the unit-cell doubling originated from the SF state through STM measurement. Although the signature of the SF state appears only dynamically in a uniform SC state, a topological defect (vortex) stabilizes static texture of the boson condensate and the spatial component of the massless internal gauge field $\mathbf{a}$[3]. We determined the texture associated with a single vortex based on a simple London model. A half flux quantum of the EM gauge field $\mathbf{A}$ penetrates over a huge region $r\lesssim\lambda_L$, as compared with a half flux quantum of the internal gauge field $\mathbf{a}$[3], which penetrates over a region $r\lesssim\lambda_a$. Although the fermions do not couple to the EM gauge field, they still see the internal gauge flux tube associated with $\mathbf{a}$[3]. Due to this reason, the topological texture shows up in the hopping (χ_{ij}) and pairing (Δ_{ij}) order parameters of the physical electrons and gives rise to the staggered modulation of χ_{ij} and Δ_{ij} through the gauge invariant ''superfluid velocity'' $\mathbf{v}$ associated with $\mathbf{a}$[3] [see Eqs. (3.5) and (3.6)].

The most important formula in this paper is Eq. (3.4), which directly tells us that whereas the center in the vortex core is a SF state, as one moves away from the core center, a correlated staggered modulation of the hopping amplitude $\tilde{\chi}_{ij}$ and pairing amplitude $\tilde{\Delta}_{ij}$ of the *physical* electrons becomes predominant over the region $l_c\lesssim r\lesssim\lambda_a$. Combining the results obtained through the gradient expansion and the uniform-$\mathbf{v}$ approximation, we concluded that the signature of the unit-cell doubling may be most prominently detected through the staggered peak-dip (SPD) structure inside the V-shaped profile measured on the bonds. The real band structure of BSCCO, in particular, the next-nearest-neighbor hopping $\tilde{t}_3$, plays a crucial role to push the energy scales of the SPD structure toward visibly finite-energy scales. The structure directly originates from unit-cell doubling, which is stabilized by the topological texture (phase winding) under the external magnetic field. In this respect, our effects have little to do with the *d*-wave symmetry of the superconducting order parameter. Our finding may be best summarized in Fig. 13.

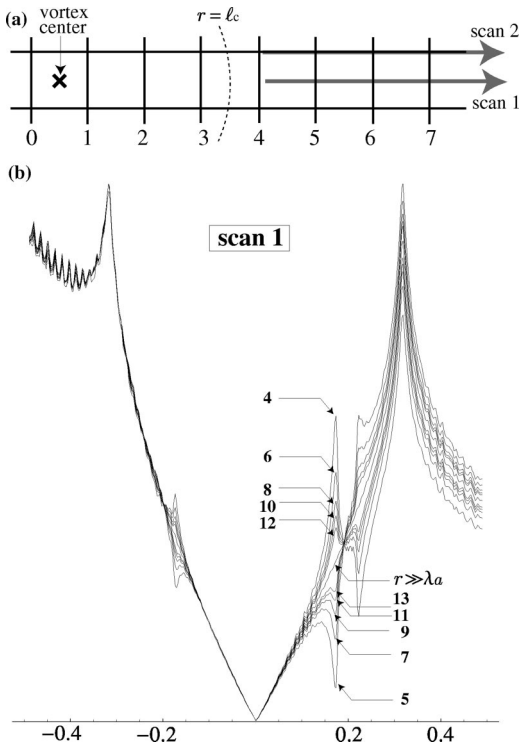

FIG. 13. (a) The best scan path to test our effects is the path denoted by ''scan 1.'' (b) The expected LDOS profile measured on the bond-center points (O sites on a CuO_2 plane) around a single SU(2) vortex with the real band structure of BSCCO being taken into account. For an illustration we assumed $l_c=3$ and $\lambda_a=10$. The staggered peak-dip (SPD) structure appears over the $l_c\lesssim r\lesssim\lambda_a$ and vanishes deep inside the *d*-wave SC state ($r\gg\lambda_a$). We expect almost no effects along the scan path denoted by ''scan 2.''

The best scan path to test our effects is shown in Fig. 13(a) as ''scan 1,'' along which the LDOS on the bonds exhibits specific peak and dip structure alternating from bond to bond in a staggered manner as indicated in Fig. 13(b) (the LDOS shown here is obtained under the same setting as in Fig. 9). The SPD structure appears over the region $l_c\lesssim r\lesssim\lambda_a$ and vanishes deep inside the *d*-wave SC state. The core size l_c presumably extends over a fermion coherence length $\xi_F\sim v_F/\Delta_0$, which may amount to a few lattice scales[25] and the energetics of a single vortex supports the fact that a large value of λ_a/l_c tends to be favored. Thus we are hopeful that there is certainly the region $l_c\lesssim r\lesssim\lambda_a$ over which our effects are detectable. Due to the lattice symmetry, the unit cell-doubling effects on the LDOS is detectable only on the bonds. Thus, we have just a typical V-shaped profile of bulk *d*-wave SC along the path denoted by ''scan 2'' in Fig. 13(a). Although the qualitative feature of the LDOS profile may not be so sensitive to the doping x in the underdoped regime, the fine detail of the SPD structure depends on the doping dependence x, which controls $a_0\propto x$ and Δ_0. In particular, existence or absence of the second peak/dip depends on x. Nevertheless, we have at least one resonance (or a pair of van Hove singularities) on the reduced zone boundary at the energy around $\omega=\pm(2\chi_0\tilde{J}\tilde{t}_3+a_0)$. [Eq. (4.30)], which always

lies inside the V-shaped profile for reasonable band-structure parameters of BSCCO.

As for an experimental setup for BSCCO sample, the best place to test our prediction is the O site around the vortex center on the CuO_2 plane. The size of the Wannier function at the O sites on Cu-O-Cu bonds is presumably an order of 10% in magnitude as compared with the nearest Cu sites. However, it is noteworthy that the STM tunneling into the O sites may take place directly via the STM tips, while the tunneling into the Cu sites on the CuO_2 plane takes place indirectly through the Bi atom on the BiO layer.[38] Thus, we are hopeful that the STM signal may more sensitively detect the LDOS profile at the O sites than at the Cu sites. We stress that the SPD structure is totally ascribable to unit-cell doubling and the robust topological texture. Therefore, we may safely say that the SPD structure survives any tunneling-matrix-element effects and can directly be detected through the STM experiment.

ACKNOWLEDGMENTS

We acknowledge Seamus Davis, Dung-Hai Lee, Naoto Nagaosa, Tai-Kai Ng, Masao Ogata, and Subir Sachdev for stimulating communications. J.K. was supported by a Monbusho Grant for overseas research during his stay at MIT P.A.L., and X.-G.W, acknowledge support by NSF under the MRSEI Program DMR 98-08491. X.-G.W. also acknowledges support by NSF Grant No. DMR 97-14198.

APPENDIX A: INTERNAL PHASE OF THE LOCAL BOSON CONDENSATE

The uniform *d*-wave SC state in the *d*-wave gauge is described by

$$U_{ij}^{d}=-\chi_0\tau^3+(-1)^{i_y+j_y}\Delta_0\tau_1, \tag{A1}$$

$$h_{0i}^{d}=\begin{pmatrix}\sqrt{x}\\0\end{pmatrix}, \tag{A2}$$

which is just equivalent to the U(1) MF solution for the *d*-wave SC state. Now, thanks to the SU(2) symmetry, the same state can be described in the SF gauge via the SU(2) gauge transformation $w_i^{\dagger}$ given by Eq. (2.10). The gauge transformation converts U_{ij}^{d} and h_{0i}^{d} to

$$U_{ij}^{\mathrm{SF}}\rightarrow w_i^{\dagger}U_{ij}^{d}w_j=-A\tau^3\exp[i(-1)^{i_x+j_y}\Phi_0\tau^3], \tag{A3}$$

$$h_{0i}^{\mathrm{SF}}\rightarrow w_i^{\dagger}h_{0i}^{d}=\sqrt{\frac{x}{2}}\begin{pmatrix}1\\-i(-1)^{i_x+i_y}\end{pmatrix}, \tag{A4}$$

where $A=\sqrt{\chi_0^2+\Delta_0^2}$ and $\Phi_0=\tan^{-1}(\Delta_0/\chi_0)$. Now, the low-energy excitations around the SC state in the SF gauge are obtained by fixing U_{ij}^{SF} and then rotating the boson condensate in the internal SU(2) space. The direction in the internal SU(2) space is specified by the internal angles ϕ and θ as in Eq. (2.12). We obtain this parameterization more directly through transforming h_{0i}^{d} by

$$g_i^{\dagger}=\exp\left[-i(-1)^{i_x+i_y}\frac{\theta_i}{2}\tau^1\right]\exp\left[-i\frac{\phi_i}{2}\tau^3\right], \tag{A5}$$

which we encounter in Sec. III A [see Eq. (3.1)] when we make a gauge transformation.

APPENDIX B: LONDON-MODEL ANALYSIS OF A SINGLE SU(2) VORTEX

Here we apply the London-model prescription[33] to a single SU(2) vortex. Plugging Eq. (2.13) into Eq. (2.16) gives $F_K=F_V+F_v$, where

$$F_V=\frac{x}{2m_b}\int d\mathbf{r}\,\mathbf{V}(\mathbf{r})^2, \tag{B1}$$

$$F_v=\frac{x}{2m_b}\int d\mathbf{r}\,v(\mathbf{r})^2, \tag{B2}$$

with

$$\mathbf{V}=\frac{1}{2}\boldsymbol{\nabla}\varphi_2-\frac{e}{c}\mathbf{A}=\boldsymbol{\nabla}\alpha-\frac{e}{c}\mathbf{A}, \tag{B3}$$

$$\mathbf{v}=\tfrac{1}{2}\boldsymbol{\nabla}\varphi_2-\mathbf{a}^3=\tfrac{1}{2}\boldsymbol{\nabla}\phi-\mathbf{a}^3, \tag{B4}$$

being the superfluid velocities associated with $\mathbf{A}$ and $\mathbf{a}^3$ fields, respectively. This decomposition indicates that $\mathbf{A}$ and $\mathbf{a}^3$ gauge fields are decoupled at the mean-field level. The stationality condition with respect to $\mathbf{A}$, $\delta(F_V+F_A)/\delta\mathbf{A}=0$, is reduced to $\boldsymbol{\nabla}^2\mathbf{H}(r)-\lambda_L^{-2}\mathbf{H}(\mathbf{r})=-(\phi_0^{\mathrm{EM}}/\lambda_L^2)\hat{\mathbf{e}}_z\delta(r)$, which gives the solution

$$\mathbf{H}(r)=\frac{\phi_0^{\mathrm{EM}}}{2\pi\lambda_L^2}\hat{\mathbf{e}}_z K_0\left(\frac{r}{\lambda_L}\right), \tag{B5}$$

where K_0 is the zero-order modified Bessel function of an imaginary argument. The London penetration depth is defined as $\lambda_L^2=m_bc^2/4\pi e^2x$. The EM unit flux is $\phi_0^{\mathrm{EM}}=hc/2e$ where we have retrieved the Planck constant. The physical supercurrent associated with $\mathbf{A}$ becomes

$$\mathbf{J}(\mathbf{r})=\frac{c}{4\pi}\boldsymbol{\nabla}\times\mathbf{H}(r)=\frac{\phi_0^{\mathrm{EM}}c}{8\pi^2\lambda_L^3}\hat{\mathbf{e}}_\phi K_1\left(\frac{r}{\lambda_L}\right), \tag{B6}$$

which globally circulates around the vortex center over the length scale λ_L.

Taking account of Eq. (2.21), the stationality condition with respect to $\mathbf{a}^3$, $\delta(F_v+F_a)/\delta\mathbf{a}^3=0$, is reduced to $-2xt\mathbf{v}(\mathbf{r})+\sigma\int d\mathbf{r}'\boldsymbol{\nabla}_r\kappa(\mathbf{r}-\mathbf{r}')\times\mathbf{h}(\mathbf{r}')=0$. Taking the curl of this equation and going to Fourier space, we obtain

$$\mathbf{h}(\mathbf{q})=\hat{\mathbf{e}}_z\frac{\phi_0^{\mathrm{gauge}}}{1+\lambda_a\kappa_{\mathbf{q}}\mathbf{q}^2}=\hat{\mathbf{e}}_z\frac{\phi_0^{\mathrm{gauge}}}{1+\lambda_a|\mathbf{q}|}, \tag{B7}$$

where we made use of Eq. (2.22). The gauge-field-penetration depth and the unit flux associated with it are given by $\lambda_a=m_b\sigma/x$ and $\phi_0^{\mathrm{gauge}}=h/2$, respectively. The Fouier transform of Eq. (B7) gives

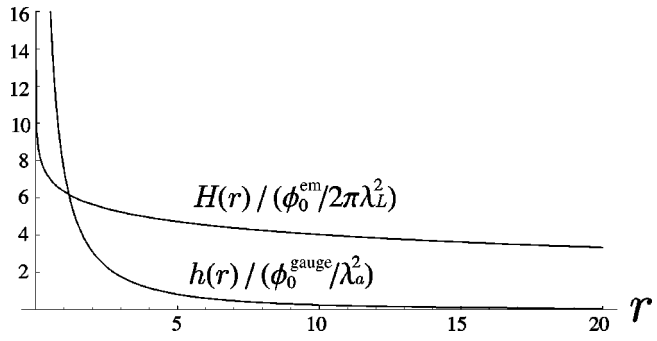

FIG. 14. Spatial dependence of $H(r)/(\phi_0^{\rm EM}/2\pi\lambda_L^2)$ and $h(r)/(\phi_0^{\rm gauge}/\lambda_a^2)$ assuming $\lambda_L/\lambda_a=50$ and $\lambda_a=10$ with lattice unit. Apparent divergence of $h(r)$ at $r=0$ should be taken as an artifact of continuum limit.

$$\mathbf{h}(r)=\frac{\phi_0^{\rm gauge}}{\lambda_\alpha^2}\hat{\mathbf{e}}_z\left[\frac{\lambda_a}{r}-\frac{\pi}{2}\left\{\mathbf{H}_0\left(\frac{r}{\lambda_a}\right)-\mathbf{N}_0\left(\frac{r}{\lambda_a}\right)\right\}\right], \quad \text{(B8)}$$

where $\mathbf{H}_0(z)$ and $\mathbf{N}_0(z)$ denote the Struve function[34] and the Bessel function of the second kind, respectively. We note that $\lambda_a/\lambda_L\sim(1/\sqrt{x})(e/c)\ll 1$, where we used $\sigma=\sqrt{\tilde{J}\Delta}\sim 1/\sqrt{m_b}$ (λ_L reaches $\sim$500 with lattice unit in BSCCO). The essential point here is that we can reasonably assume that the EM gauge field **H** extends much broader than the internal gauge field **h**. Under this circumstance, the effect of the EM gauge potential **A** is negligible as compared with the internal gauge potential $\mathbf{a}^3$. That is to say, in our vortex model, a half flux quantum of the EM gauge field **A** penetrates over a huge region $r\lesssim\lambda_L$, as compared with a half flux quantum of the internal gauge field $\mathbf{a}^3$, which penetrates over a region $r\lesssim\lambda_a$. In Fig. 14, we show spatial decay of $H(r)/(\phi_0^{\rm EM}/2\pi\lambda_L^2)$ and $h(r)/(\phi_0^{\rm gauge}/\lambda_a^2)$ assuming $\lambda_L/\lambda_a=50$ and $\lambda_a=10$ with lattice unit. The apparent divergence of $h(r)$ at $r=0$ should be taken as an artifact of the continuum limit, since there is natural cutoff of an order of the inverse lattice scale.

We shall now argue how λ_a can become larger than l_c in terms of energetics of a single vortex. The energy associated with a single vortex consists of the following contribution: the cost for the SF core formation $\epsilon_{\rm core}$, the electromagnetic contribution $\epsilon_{\rm EM}=F_V+F_A$, and the contribution of the internal gauge field $\epsilon_{\rm gauge}=F_v+F_a$. The energy cost for the SF core formation is estimated as[27] $\epsilon_{\rm core}\sim\sqrt{\tilde{J}\Delta}l_c^2x^{3/2}$, which favors smaller l_c. On the other hand, the core size cannot be smaller than $x^{-1/2}$ without costing too much kinetic energy. Thus, we conclude that the SF core occupies a radius of $l_c\sim x^{-1/2}$ at the MF level. In the present scheme, it is quite reasonable to expect that as the doping x decreases, the core size becomes larger because the energy difference between the SC and the SF state decreases as $x\to 0$.

The electromagnetic contribution comes from $\epsilon_{\rm EM}=F_V+F_A$, which reduces to[33]

$$\epsilon_{\rm EM}=\frac{1}{8\pi}\int_{r>l_c}d\mathbf{r}[\mathbf{H}^2+\lambda_L^2(\nabla\times\mathbf{H})^2]=\frac{\pi x}{4m_b}\ln\frac{\lambda_L}{l_c}. \quad \text{(B9)}$$

To compute $\epsilon_{\rm gauge}$, we first take the curl of Eq. (B4) and go to the Fourier space to obtain

$$\mathbf{v}(\mathbf{q})=-i\pi\frac{\mathbf{q}\times\hat{\mathbf{e}}_z}{q^2}\frac{\lambda_a q}{1+\lambda_a q}, \quad \text{(B10)}$$

and similarly

$$\mathbf{a}^3(\mathbf{q})=-i\pi\frac{\mathbf{q}\times\hat{\mathbf{e}}_z}{q^2}\frac{1}{1+\lambda_a q} \quad \text{(B11)}$$

Recalling $x/2m_b=\sigma/2\lambda_a$, we have

$$\epsilon_{\rm gauge}=\frac{\pi^2\sigma}{2}\sum_{\mathbf{q}}\frac{1}{q}\frac{1}{1+\lambda_a q}=\frac{\pi\sigma}{2\lambda_a}\ln\frac{\lambda_a}{l_c}. \quad \text{(B12)}$$

We thus have the energy cost associated with a single vortex,

$$\epsilon_{\rm vortex}=\epsilon_{\rm core}+\epsilon_{\rm gauge}+\epsilon_{\rm EM}\sim\sqrt{\tilde{J}\Delta}l_c^2x^{3/2}+\frac{\sigma\pi}{2\lambda_a}\ln\frac{\lambda_a}{l_c}+\frac{\pi x}{4m_b}\ln\frac{\lambda_L}{l_c}. \quad \text{(B13)}$$

This result is consistent with a little bit more qualitative discussion,[27] i.e., a standard $hc/2e$ vortex is possible with the SF core, which does not cost too much energy as $x\to 0$. The SF core size l_c would like to be as small as possible with the lower bound $l_c\sim x^{-1/2}$, while the size of the gauge-field distribution $\lambda_a=m_b\sigma/x$ would like to be large.

APPENDIX C: COMPUTATION OF LDOS

1. Derivation of Eq. (4.14)

We start with Eq. (4.3). The LDOS at the plaquette-center, site-top, and bond-center points, as indicated in Fig. 6, are given by

$$N^{\rm plaquette}(\mathbf{r}_C,\omega)=-\frac{2x\alpha_C^2}{\pi}{\rm Im}\sum_{i,j=1,2,4,5}[\mathcal{G}_{ij}^F(i\omega)]_{11}|_{i\omega\to\omega+i\delta}, \quad \text{(C1)}$$

$$N^{\rm site}(\mathbf{r}_1,\omega)=-\frac{2x}{\pi}{\rm Im}[\mathcal{G}_{11}^F(i\omega)]_{11}|_{i\omega\to\omega+i\delta}, \quad \text{(C2)}$$

$$N^{\rm bond}(\mathbf{r}_B,\omega)=-\frac{2x\alpha_B^2}{\pi}{\rm Im}\sum_{i,j=1,2}[\mathcal{G}_{ij}^F(i\omega)]_{11}|_{i\omega\to\omega+i\delta}, \quad \text{(C3)}$$

respectively. The envelope function is simulated by $\alpha_i(\mathbf{r})=\epsilon^{-|\mathbf{r}-\mathbf{r}_i|/\xi}$ ($\xi=\frac{1}{2}$ with lattice unit) in the bond direction. Tuning $\alpha_i(\mathbf{r}_i)=1$ at the site-top points, we put $\alpha_1(\mathbf{r}_C)=\alpha_2(\mathbf{r}_C)=\alpha_4(\mathbf{r}_C)=\alpha_5(\mathbf{r}_C)\sim e^{-1}\equiv\alpha_C$, and $\alpha_1(\mathbf{r}_B)=\alpha_2(\mathbf{r}_B)\equiv\alpha_B$. Using Eq. (4.11), we obtain

$$\psi_1+\psi_2+\psi_4+\psi_5=\frac{4}{\sqrt{2}}\sum_{\mathbf{k}\in{\rm RZ}}e^{i\mathbf{k}\cdot\mathbf{r}_C}\left[\cos\frac{k_x}{2}\cos\frac{k_y}{2}\psi_{\mathbf{k}}\pm\sin\frac{k_x}{2}\sin\frac{k_y}{2}\psi_{\mathbf{k}+\mathbf{Q}}\right], \quad \text{(C4)}$$

$$\psi_1=\frac{1}{\sqrt{2}}\sum_{k\in \mathrm{RZ}} e^{i\mathbf{k}\cdot\mathbf{r}_1}[\psi_{\mathbf{k}}\pm\psi_{\mathbf{k}+\mathbf{Q}}], \tag{C5}$$

$$\psi_1+\psi_2=\frac{2}{\sqrt{2}}\sum_{k\in \mathrm{RZ}} e^{i\mathbf{k}\cdot\mathbf{r}_B}\left[\cos\frac{k_x}{2}\psi_{\mathbf{k}}\pm i\sin\frac{k_x}{2}\psi_{\mathbf{k}+\mathbf{Q}}\right] \tag{C6}$$

where $-$ and $+$ signs are for the cases where the site 1 belongs to the A and B sites, respectively. Constructing the propagators with these wave functions, we obtain a formula, Eq. (4.14), in a concrete form. For example, in Eq. (C3) we obtan

$$\sum_{i,j=1,2}\mathcal{G}^F_{ij}=\mathcal{G}^F(\mathbf{r}_B,i\omega)\pm\delta\mathcal{G}^F(\mathbf{r}_B,i\omega). \tag{C7}$$

The uniform and staggered counterparts are computed as

$$\begin{aligned}\mathcal{G}^F(\mathbf{r}_B,i\omega)=&\sum_{\mathbf{k}\in \mathrm{RZ}}\sum_{\mathbf{k}'\in \mathrm{RZ}} e^{i(\mathbf{k}-\mathbf{k}')\cdot\mathbf{r}_B}\\ &\times\left[\cos\frac{k_x}{2}\cos\frac{k'_x}{2}\mathcal{G}^F(\mathbf{k},\mathbf{k}',i\omega)\right.\\ &\left.+\sin\frac{k_x}{2}\sin\frac{k'_x}{2}\mathcal{G}^F(\mathbf{k}+\mathbf{Q},\mathbf{k}'+\mathbf{Q},i\omega)\right]\\ =&\sum_k\cos^2\frac{k_x}{2}\mathcal{G}^F_0(\mathbf{k},i\omega)\end{aligned} \tag{C8}$$

and

$$\begin{aligned}\delta\mathcal{G}^F(\mathbf{r}_B,i\omega)=&i\sum_{\mathbf{k}\in \mathrm{RZ}}\sum_{\mathbf{k}'\in \mathrm{RZ}} e^{i(\mathbf{k}-\mathbf{k}')\cdot\mathbf{r}_B}\\ &\times\left[\cos\frac{k_x}{2}\sin\frac{k'_x}{2}\mathcal{G}^F(\mathbf{k},\mathbf{k}'+\mathbf{Q},i\omega)\right.\\ &\left.-\sin\frac{k_x}{2}\cos\frac{k'_x}{2}\mathcal{G}^F(\mathbf{k}+\mathbf{Q},\mathbf{k}',i\omega)\right]\\ =&\sum_{\mathbf{k}\in \mathrm{RZ}}\sum_{\mathbf{q}\sim\mathrm{small}}\sin(\mathbf{q}\cdot\mathbf{r}_B)\sin\frac{k_x+\frac{\mathbf{q}_x}{2}}{2}\cos\frac{k_x-\frac{\mathbf{q}_x}{2}}{2}\\ &\times\left[\mathcal{G}^F\left(\mathbf{k}-\frac{\mathbf{q}}{2};\mathbf{k}+\frac{\mathbf{q}}{2}+\mathbf{Q},i\omega\right)\right.\\ &\left.+\mathcal{G}^F\left(\mathbf{k}+\frac{\mathbf{q}}{2}+\mathbf{Q},\mathbf{k}-\frac{\mathbf{q}}{2},i\omega\right)\right],\end{aligned} \tag{C9}$$

which give Eqs. (4.15) and (4.20), respectively. At the last step we replaced $\mathbf{k}-\mathbf{k}'$ and $(\mathbf{k}+\mathbf{k}')/2$ with $\mathbf{q}$ and $\mathbf{k}$, respectively.

2. Computation of the generalized propagators

Next we compute

$$\mathcal{G}^F\left(\mathbf{k}+\frac{\mathbf{q}}{2}+\mathbf{Q},\mathbf{k}-\frac{\mathbf{q}}{2},\tau\right)=-\langle T_r\psi_{\mathbf{k}+\mathbf{q}/2+\mathbf{Q}}(\tau)\psi^\dagger_{\mathbf{k}-\mathbf{q}/2}\rangle, \tag{C10}$$

$$\mathcal{G}^F\left(\mathbf{k}-\frac{\mathbf{q}}{2},\mathbf{k}+\frac{\mathbf{q}}{2}+\mathbf{Q},\tau\right)=-\langle T_r\psi_{\mathbf{k}-\mathbf{q}/2}(\tau)\psi^\dagger_{\mathbf{k}+\mathbf{q}/2+\mathbf{Q}}\rangle \tag{C11}$$

at the Born level. First, we rewrite the perturbation term (4.7) in momentum space,

$$\begin{aligned}\delta H^F=&-i\tilde{J}\sum_{\mathbf{k}\in \mathrm{RZ}}\sum_{\mathbf{k}'\in \mathrm{RZ}}\sin\left(\frac{k_x+k'_x}{2}\right)v_x(\mathbf{k}-\mathbf{k}')[\psi^\dagger_{\mathbf{k}}(\Delta_0\tau^3\\ &+\chi_0\tau^1)\psi_{\mathbf{k}'+\mathbf{Q}}-\psi^\dagger_{\mathbf{k}+\mathbf{Q}}(\Delta_0\tau^3+\chi_0\tau^1)\psi_{\mathbf{k}'}]\\ &+iJ\sum_{\mathbf{k}\in \mathrm{RZ}}\sum_{\mathbf{k}'\in \mathrm{RZ}}\sin\left(\frac{k_y+k'_y}{2}\right)v_y(\mathbf{k}-\mathbf{k}')[\psi^\dagger_{\mathbf{k}}(\Delta_0\tau^3\\ &-\chi_0\tau^1)\psi_{\mathbf{k}'+\mathbf{Q}}-\psi^\dagger_{\mathbf{k}+\mathbf{Q}}(\Delta_0\tau^2-\chi_0\tau^1)\psi_{\mathbf{k}'}].\end{aligned} \tag{C12}$$

By replacing $\mathbf{k}-\mathbf{k}'$ and $(\mathbf{k}+\mathbf{k}')/2$ with $\mathbf{q}$ and $\mathbf{k}$, respectively, and recalling Eq. (B10), we reach Eq. (4.12). The first-order contribution of δH^F to the propagator is obtained as

$$\begin{aligned}\mathcal{G}^F\left(\mathbf{k}+\frac{\mathbf{q}}{2}+\mathbf{Q},\mathbf{k}-\frac{\mathbf{q}}{2},\tau\right)=&-\sum_\omega e^{i\omega\tau}\mathcal{G}^F_0\left(\mathbf{k}+\frac{\mathbf{q}}{2}+\mathbf{Q},i\omega\right)\\ &\times C_{\mathbf{k}+\mathbf{Q}}(\mathbf{q})\mathcal{G}^F_0\left(\mathbf{k}-\frac{\mathbf{q}}{2},i\omega\right),\end{aligned} \tag{C13}$$

i.e.,

$$\begin{aligned}\mathcal{G}^F\left(\mathbf{k}+\frac{\mathbf{q}}{2}+\mathbf{Q},\mathbf{k}-\frac{\mathbf{q}}{2},i\omega\right)=&-\mathcal{G}^F_0\left(\mathbf{k}+\frac{\mathbf{q}}{2}+\mathbf{Q},i\omega\right)C_{\mathbf{k}}(\mathbf{q})\\ &\times\mathcal{G}^F_0\left(\mathbf{k}-\frac{\mathbf{q}}{2},i\omega\right).\end{aligned} \tag{C14}$$

Similarly, we obtain

$$\begin{aligned}\mathcal{G}^F\left(\mathbf{k}-\frac{\mathbf{q}}{2},\mathbf{k}+\frac{\mathbf{q}}{2}+\mathbf{Q},\tau\right)=&-\mathcal{G}^F_0\left(\mathbf{k}-\frac{\mathbf{q}}{2},i\omega\right)C_{\mathbf{k}}(\mathbf{q})\\ &\times\mathcal{G}^F_0\left(\mathbf{k}+\frac{\mathbf{q}}{2}+\mathbf{Q},i\omega\right).\end{aligned} \tag{C15}$$

Recalling Eq. (4.8), we explicitly write down perturbative corrections,

$$\mathcal{G}^F\left(\mathbf{k}-\frac{\mathbf{q}}{2},\mathbf{k}+\frac{\mathbf{q}}{2}+\mathbf{Q},i\omega\right)+\mathcal{G}^F\left(\mathbf{k}+\frac{\mathbf{q}}{2}+\mathbf{Q},\mathbf{k}-\frac{\mathbf{q}}{2},i\omega\right)$$
$$=-\frac{1}{i\omega-E_+}\frac{1}{i\omega-E_-}[U_+C_{\mathbf{k}}(\mathbf{q})U_-+U_-C_{\mathbf{k}}(\mathbf{q})U_+]$$
$$-\frac{1}{i\omega+E_+}\frac{1}{i\omega+E_-}[V_+C_{\mathbf{k}}(\mathbf{q})V_-+V_-C_{\mathbf{k}}(\mathbf{q})V_+]$$
$$-\frac{1}{i\omega-E_+}\frac{1}{i\omega+E_-}[U_+C_{\mathbf{k}}(\mathbf{q})V_-+V_-C_{\mathbf{k}}(\mathbf{q})U_+]$$
$$-\frac{1}{i\omega+E_+}\frac{1}{i\omega-E_+}[V_+C_{\mathbf{k}}(\mathbf{q})U_-+U_-C_{\mathbf{k}}(\mathbf{q})V_+], \tag{C16}$$

where

$$E_+=E_{\mathbf{k}+\mathbf{q}/2+\mathbf{Q}},\quad E_-=E_{\mathbf{k}-\mathbf{q}/2}, \tag{C17}$$
$$U_\pm=\tfrac{1}{2}[1+\gamma_\pm\tau^3+\eta_\pm\tau^1],$$
$$V_\pm=\tfrac{1}{2}[1-\gamma_\pm\tau^3-\eta_\pm\tau^1], \tag{C18}$$

with $\gamma_+=\gamma_{\mathbf{k}+\mathbf{q}/2+\mathbf{Q}}/E_{\mathbf{k}+\mathbf{q}/2+\mathbf{Q}}$, $\gamma_-=\gamma_{\mathbf{k}-\mathbf{q}/2}/E_{\mathbf{k}-\mathbf{q}/2}$, $\eta_+=\eta_{\mathbf{k}+\mathbf{q}+\mathbf{Q}}/E_{\mathbf{k}+\mathbf{q}/2+\mathbf{Q}}$, and $\eta_-=\eta_{\mathbf{k}-\mathbf{q}/2}/E_{\mathbf{k}-\mathbf{q}/2}$. Taking the 11 component of Eq. (C16) and then performing analytic continuation, $i\omega\rightarrow\omega+i\delta$, we reach Eq. (4.24).

APPENDIX D: EXPLICIT FORM OF $\mathbf{G}^F$

By simply taking inverse of the matrix $i\omega\mathbf{1}-\mathbf{T}_{\mathbf{k}}$ with $\mathbf{T}_{\mathbf{k}}$ given by Eq. (4.34), we obtain an explicit form of $\mathbf{G}^F(\mathbf{k},i\omega)$. The 11 and 33 components are given by

$$[\mathbf{G}^F(\mathbf{k},i\omega)]_{11}=[\mathbf{G}(\mathbf{k}+\mathbf{Q},i\omega)]_{33}$$
$$=\frac{(i\omega)^3+A_{\mathbf{k}}(i\omega)^2-B_{\mathbf{k}}i\omega-C_{\mathbf{k}}}{D(\mathbf{k},i\omega)} \tag{D1}$$
$$=\frac{U_{1\mathbf{k}}}{i\omega-E_{\mathbf{k}}^-}+\frac{V_{1\mathbf{k}}}{i\omega+E_{\mathbf{k}}^-}+\frac{U_{2\mathbf{k}}}{i\omega-E_{\mathbf{k}}^+}+\frac{V_{2\mathbf{k}}}{i\omega+E_{\mathbf{k}}^+}, \tag{D2}$$

where $D(\mathbf{k},i\omega)=\det[i\omega-\mathbf{T}_{\mathbf{k}}]=(i\omega-E_{\mathbf{k}}^-)(i\omega+E_{\mathbf{k}}^-)(i\omega-E_{\mathbf{k}}^+)(i\omega+E_{\mathbf{k}}^+)$, and

$$A_{\mathbf{k}}=a_{\mathbf{k}}-\gamma_{\mathbf{k}}, \tag{D3}$$
$$B_{\mathbf{k}}=(a_{\mathbf{k}}+\gamma_{\mathbf{k}})^2+\eta_{\mathbf{k}}^2+\lambda_{\mathbf{k}}^2+\mu_{\mathbf{k}}^2 \tag{D4}$$
$$C_{\mathbf{k}}=(a_{\mathbf{k}}+\gamma_{\mathbf{k}})(a_{\mathbf{k}}^2-\gamma_{\mathbf{k}}^2-\lambda_{\mathbf{k}}^2+\mu_{\mathbf{k}}^2)+(a_{\mathbf{k}}-\gamma_{\mathbf{k}})\eta_{\mathbf{k}}^2+2\eta_{\mathbf{k}}\lambda_{\mathbf{k}}\mu_{\mathbf{k}}. \tag{D5}$$

The generalized coherence factors are given by

$$U_{1\mathbf{k}}=\frac{1}{2}\frac{1}{P_{\mathbf{k}}}[(E_{\mathbf{k}}^-)^2+E_{\mathbf{k}}^-A_{\mathbf{k}}-B_{1\mathbf{k}}-C_{1\mathbf{k}}/E_{\mathbf{k}}^-], \tag{D6}$$
$$V_{1\mathbf{k}}=\frac{1}{2}\frac{1}{P_{\mathbf{k}}}[(E_{\mathbf{k}}^-)^2-E_{\mathbf{k}}^-A_{\mathbf{k}}-B_{\mathbf{k}}+C_{\mathbf{k}}/E_{\mathbf{k}}^-], \tag{D7}$$
$$U_{2\mathbf{k}}=\frac{1}{2}\frac{1}{P_{\mathbf{k}}}[-(E_{\mathbf{k}}^+)^2-E_{\mathbf{k}}^+A_{\mathbf{k}}+B_{\mathbf{k}}+C_{\mathbf{k}}/E_{\mathbf{k}}^+], \tag{D8}$$
$$V_{2\mathbf{k}}=\frac{1}{2}\frac{1}{P_{\mathbf{k}}}[-(E_{\mathbf{k}}^+)^2+E_{\mathbf{k}}^+A_{\mathbf{k}}+B_{\mathbf{k}}-C_{\mathbf{k}}/E_{\mathbf{k}}^+], \tag{D9}$$

where

$$P_{\mathbf{k}}\equiv(E_{\mathbf{k}}^-)^2-(E_{\mathbf{k}}^+)^2=-4\sqrt{a_{\mathbf{k}}^2(\gamma_{\mathbf{k}}^2+\lambda_{\mathbf{k}}^2)+(\eta_{\mathbf{k}}\lambda_{\mathbf{k}}+\gamma_{\mathbf{k}}\mu_{\mathbf{k}})^2}. \tag{D10}$$

Similarly,

$$[\mathbf{G}^F(\mathbf{k},i\omega)]_{13}$$
$$=[\mathbf{G}^F(\mathbf{k},i\omega)]_{31}^*$$
$$=-i\lambda_{\mathbf{k}}\frac{(i\omega)^2+2u_{\mathbf{k}}i\omega+\tilde{C}_{\mathbf{k}}}{D(\mathbf{k},i\omega)}$$
$$=-i\lambda_{\mathbf{k}}\left[\frac{\tilde{U}_{1\mathbf{k}}}{i\omega-E_{\mathbf{k}}^-}+\frac{\tilde{V}_{1\mathbf{k}}}{i\omega+E_{\mathbf{k}}^-}+\frac{\tilde{U}_{2\mathbf{k}}}{i\omega-E_{\mathbf{k}}^+}+\frac{\tilde{V}_{2\mathbf{k}}}{i\omega+E_{\mathbf{k}}^+}\right], \tag{D11}$$

where

$$\tilde{C}_{\mathbf{k}}=a_{\mathbf{k}}^2-\gamma_{\mathbf{k}}^2-\lambda_{\mathbf{k}}^2+\eta_{\mathbf{k}}^2-\mu_{\mathbf{k}}^2+2\gamma_{\mathbf{k}}\eta_{\mathbf{k}}\mu_{\mathbf{k}}/\lambda_{\mathbf{k}}, \tag{D12}$$
$$\tilde{U}_{1\mathbf{k}}=-\frac{1}{2}\frac{1}{P_{\mathbf{k}}}[E_{\mathbf{k}}^-+2a_{\mathbf{k}}+\tilde{C}_{\mathbf{k}}/E_{\mathbf{k}}^-], \tag{D13}$$
$$\tilde{V}_{1\mathbf{k}}=-\frac{1}{2}\frac{1}{P_{\mathbf{k}}}[-E_{\mathbf{k}}^-+2a_{\mathbf{k}}-\tilde{C}_{\mathbf{k}}/E_{\mathbf{k}}^-], \tag{D14}$$
$$\tilde{U}_{2\mathbf{k}}=-\frac{1}{2}\frac{1}{P_{\mathbf{k}}}[-E_{\mathbf{k}}^+-2a_{\mathbf{k}}-\tilde{C}_{\mathbf{k}}/E_{\mathbf{k}}^+], \tag{D15}$$
$$\tilde{V}_{2\mathbf{k}}=-\frac{1}{2}\frac{1}{P_{\mathbf{k}}}[E_{\mathbf{k}}^+-2a_{\mathbf{k}}+\tilde{C}_{\mathbf{k}}/E_{\mathbf{k}}^+]. \tag{D16}$$

Now, LDOS at the midpoint on the bond connecting $\mathbf{r}_i$ and $\mathbf{r}_i+\hat{\mathbf{e}}_\mu$ is given in the form of Eq. (4.38) with

$$\tilde{N}_0(\omega)=\sum_{\mathbf{k}}\cos^2\frac{k_\mu}{2}[U_{1\mathbf{k}}\delta(\omega-E_{\mathbf{k}}^-)+V_{1\mathbf{k}}\delta(\omega+E_{\mathbf{k}}^-)$$
$$+U_{2\mathbf{k}}\delta(\omega-E_{\mathbf{k}}^+)+V_{2\mathbf{k}}\delta(\omega+E_{\mathbf{k}}^+)], \tag{D17}$$

$$\delta\tilde{N}(\omega)=\sum_{\mathbf{k}\in RZ}\lambda_{\mathbf{k}}\sin k_\mu[\tilde{U}_{1\mathbf{k}}\delta(\omega-E_{\mathbf{k}}^-)+\tilde{V}_{1\mathbf{k}}\delta(\omega+E_{\mathbf{k}}^-)$$
$$+\tilde{U}_{2\mathbf{k}}\delta(\omega-E_{\mathbf{k}}^+)+\tilde{V}_{2\mathbf{k}}\delta(\omega+E_{\mathbf{k}}^+)] \tag{D18}$$

These equations further reduce to Eqs. (4.44) and (4.45).

[1] P. W. Anderson, Science **235**, 1196 (1987).
[2] I. Affleck and J. B. Marston, Phys. Rev. B **37**, 3774 (1988).
[3] G. Kotoliar and J. Liu, Phys. Rev. B **38**, 5142 (1988).
[4] Y. Suzumura, Y. Hasegawa, and H. Fukuyama, J. Phys. Soc. Jpn. **57**, 2768 (1988).
[5] G. Baskaran and P. W. Anderson, Phys. Rev. B **37**, 580 (1988).
[6] L. B. Ioffe and A. I. Larkin, Phys. Rev. B **39**, 8988 (1989).
[7] P. A. Lee and N. Nagaosa, Phys. Rev. B **46**, 5621 (1992).
[8] I. Affleck, Z. Zou, T. Hsu, and P. W. Anderson, Phys. Rev. B **38**, 745 (1988).
[9] D. Poilblanc and Y. Hasegawa, Phys. Rev. B **41**, 6989 (1990).
[10] M. U. Ubbens and P. A. Lee, Phys. Rev. B **46**, 8434 (1992).
[11] H. Fukuyama, Prog. Theor. Phys. Suppl. **108**, 287 (1992).
[12] X.-G. Wen and P. A. Lee, Phys. Rev. Lett. **76**, 503 (1996).
[13] P. A. Lee, N. Nagaosa, T. K. Ng, and X.-G. Wen, Phys. Rev. B **57**, 6003 (1998).
[14] D. A. Ivanov, P. A. Lee, and X.-G. Wen, Phys. Rev. Lett. **84**, 3958 (2000).
[15] P. W. Leung, Phys. Rev. B **62**, R6112 (1988).
[16] S. H. Pan, E. W. Hudson, and J. C. Davis, Rev. Sci. Instrum. **70**, 1459 (1999).
[17] I. Maggio-Aprile, Ch. Renner, A. Erb, E. Walker, and Ø. Fisher, Phys. Rev. Lett. **75**, 2754 (1995).
[18] Ch. Renner, B. Revaz, K. Kadowaki, I. Maggio-Aprile, and O. Fischer, Phys. Rev. Lett. **80**, 3606 (1998).
[19] S. H. Pan, E. W. Hudson, A. K. Gupta, K.-W. Ng, H. Eisaki, S. Uchida, and J. C. Davis, Phys. Rev. Lett. **85**, 1536 (2000).
[20] N. Nagaosa and P. A. Lee, Phys. Rev. B **45**, 966 (1992).
[21] S. Sachdev, Phys. Rev. B **45**, 389 (1992).
[22] A. Himeda, M. Ogata, Y. Tanaka, and S. Kashiwaya, J. Phys. Soc. Jpn. **66**, 3367 (1997).
[23] H. Tsuchiura, Y. Tanaka, M. Ogata, and S. Kashiwaya, J. Phys. Soc. Jpn. **68**, 2510 (1999).
[24] M. Franz and Z. Tešanović, Phys. Rev. B **63**, 064516 (2001).
[25] J. H. Han, Q.-H. Wang, and D.-H. Lee, cond-mat/0012450 (unpublished).
[26] Q.-H. Wang, J. H. Han, and D.-H. Lee, Phys. Rev. B **64**, 064512 (2001).
[27] P. A. Lee and X.-G. Wen, Phys. Rev. B **63**, 224517 (2001).
[28] T. Hsu, J. B. Marston, and I. Affleck, Phys. Rev. B **43**, 2866 (1991).
[29] J. Kishine, P. A. Lee, and X.-G. Wen, Phys. Rev. Lett. **86**, 5365 (2001).
[30] E. Dagotto, E. Fradkin, and A. Moreo, Phys. Rev. B **38**, 2926 (1998).
[31] X.-G. Wen, Phys. Rev. B **44**, 2664 (1991).
[32] When we write Eq. (2.9) as

$$U_{ij}^{\mathrm{SE}}=\begin{pmatrix} -\chi_{ij}^{\mathrm{SF}} & 0 \\ 0 & \chi_{ij}^{\mathrm{SF}} \end{pmatrix},$$

an additional gauge transformation $\chi_{ij}^{\mathrm{SF}}\rightarrow i\chi_{ij}^{\mathrm{SF}}$ and $\chi_{ij}^{\mathrm{SF}*}\rightarrow -i\chi_{ij}^{\mathrm{SF}*}$ leads to an alternative gauge choice: $\hat{U}_{ij}^{\mathrm{SF}}=-i\chi_0-(-1)^{i_x+j_y}\tau^3\Delta_0$, which was used in the papers by Lee, Nagaosa, Ng, and Wen (Ref. 13) and Lee and Wen (Ref. 27). This gauge transformation just causes $(\pi/2, \pi/2)$ shift of the Borillouin zone and leads to the b_1 and b_2 boson bands having the same minimum at $(\pi/2, \pi/2)$. Then, the local boson condensate is written as $\hat{h}_i^{\mathrm{SF}}=\sqrt{x}\exp[-i(i_x+i_y)\pi/2]\binom{z_{i1}}{z_{i2}}$, instead of Eq. (2.12). This change of the gauge choice is of course just apparent and does not change any physical consequence of our vortex model.
[33] A. L. Fetter and P. C. Hohenberg, in *Superconductivity*, edited by R. D. Parks (Dekker, New York, 1969), Vol. 1, p. 833.
[34] The following formula is useful to evaluate the Fourier, transform of Eq. (B7):

$$\int_0^\infty \frac{xJ_0(ax)}{1+x}dx=\frac{1}{a}-\frac{\pi}{2}[\mathbf{H}_0(a)-\mathbf{N}_0(a)] \quad \text{for } a>0,$$

where $\mathbf{H}_0(z)$ and $\mathbf{N}_0(z)$ denote the Struve function and the Bessel function of the second kind, respectively.
[35] To have some feeling of this situation, we consider noninteracting electrons on a linear chain described by a toy Hamiltonian $H=-\Sigma_i[t+(-1)^i\delta][c_{i+1}^\dagger e^{i(-1)^{r_i}\phi}c_i+\mathrm{H.c.}]$. It is easy to see that the staggered orbital currents flow on bonds, $j_{ij}=it(c_{j\sigma}^\dagger c_{i\sigma}-c_{i\sigma}^\dagger c_{j\sigma})$, if $\delta=0$ and $\phi\neq 0$, while the LDOS on the bonds may become staggering if $\delta\neq 0$ and $\phi=0$. The orbital current flowing and the staggered LDOS are complementary to each other.
[36] M. R. Norman, H. Ding, M. Randeria, J. C. Campuzano, T. Yokoya, T. Takeuchi, T. Takahashi, T. Mochiku, K. Kadowaki, P. Guptasrma, and D. G. Hinks, Nature (London) **392**, 157 (1998).
[37] W. Rantner and X.-G. Wen, Phys. Rev. Lett. **85**, 3692 (2000).
[38] J.-X. Zhu, C. S. Ting, and C.-R. Hu, Phys. Rev. B **62**, 6027 (2000).